

THESIS FOR THE DEGREE OF DOCTOR OF PHILOSOPHY  
IN  
THERMO AND FLUID DYNAMICS

Transonic flow: large eddy  
simulation, numerical methods and  
subgrid modeling

CHRISTIAN WOLLBLAD

Division of Fluid Dynamics

Department of Applied Mechanics

CHALMERS UNIVERSITY OF TECHNOLOGY

Göteborg, Sweden, 2006

**Transonic flow: large eddy simulation, numerical  
methods and subgrid modeling**

**CHRISTIAN WOLLBLAD**

ISBN 91-7291-862-4

© CHRISTIAN WOLLBLAD, 2006

Doktorsavhandling vid Chalmers tekniska högskola  
Ny serie nr 2543  
ISSN 0346-718X

Department of Applied Mechanics  
Division of Fluid Dynamics  
Chalmers University of Technology  
SE-412 96 Göteborg  
Sweden

Phone: +46-(0)31-772 1400

Fax: +46-(0)31-180976

Printed at Chalmers Reproservice  
Göteborg, Sweden, 2006

# **Transonic flow: large eddy simulation, numerical methods and subgrid modeling**

**Christian Wollblad**

Division of Fluid Dynamics  
Department of Applied Mechanics  
Chalmers University of Technology

## **Abstract**

Shock wave turbulent boundary layer interactions (SWTBLI) commonly arise in turbomachinery and aerospace applications and on the exterior of high speed aircrafts. In all these cases, SWTBLI can significantly change the flow and hence the physical load imposed by it. Despite numerous experimental investigations, only a basic understanding of SWTBLI has been achieved. The bulk of the existing calculations are from Reynolds averaged Navier-Stokes computations since the high computational cost has long hindered more advanced and accurate calculations. This thesis deals with large eddy simulations of SWTBLI to develop numerical methods and subgrid models and to gain a deeper understanding of the phenomenon.

A semi-implicit preconditioning scheme has been developed. It utilizes the high aspect ratio of the cells close to the walls to decouple the implicit time stepping formulation in all but the wall-normal direction. The scheme allows the otherwise explicit Runge-Kutta scheme to take five times larger time steps than is possible with a pure explicit scheme. The scheme reduces the computational time by 60 % without any reduction in the accuracy of the calculations.

It is shown that large scale movement of the whole shock is not a local phenomenon. For strong enough shocks, elliptic leakage can trigger movement of the part of the shock closest to the wall. This movement has however no direct relation to the bursting events of the boundary layer approaching the shock. It is also shown that strong separation can occur without triggering any shock motion at all.

A zonal hybrid method for computation of wall-bounded flows was developed. Data from a direct numerical simulation of channel flow at Reynolds number 500 were filtered and the subgrid stresses expanded in a series using proper orthogonal decomposition. The series was truncated. A feed forward neural network was trained to estimate the coefficient of the series. The neural network and the orthonormal base from the expansion were applied together with a Smagorinsky subgrid model to channel flow at Reynolds number 500 with good results. Generalization to higher Reynolds numbers is briefly discussed.

**Keywords:** Transonic flow, shock wave/turbulent boundary layer interaction, LES, semi-implicit numerical scheme, SGS modeling



# List of publications

This thesis is based on the work contained in the following papers.

## Paper I

C. Wollblad, L. E. Eriksson and L. Davidson,  
“Semi-implicit Preconditioning for Wall-bounded Flow.”,  
34th AIAA Fluid Dynamics Conference and Exhibit, AIAA 2004-2135  
Portland, Oregon, 2004.

## Paper II

C. Wollblad, L. Davidson and L. E. Eriksson,  
“Large Eddy Simulation of Transonic Flow with Shock Wave/Turbulent  
Boundary Layer Interaction.”,  
AIAA Journal, Vol. 44, No. 10, 2006, pp. 2340–2353

## Paper III

C. Wollblad, L. Davidson and L. E. Eriksson,  
“Investigation of large scale shock movement in transonic flow”,  
submitted to AIAA Journal, 2006

## Paper IV

C. Wollblad and L. Davidson,  
“POD based reconstruction of subgrid stresses for wall bounded flows  
using neural networks”  
5th International Symposium on Turbulence, Heat and Mass Transfer  
Dubrovnik, Croatia, 2006.



# Acknowledgments

This work has been a great challenge for me, but probably also for my supervisors Lars Davidson and Lars-Erik Eriksson who for five years had to deal with a rather stubborn student; me. Thank you both for believing in me and for giving me the opportunity to complete this work. Thank you also for sharing some of your profound knowledge and experience.

I wish to thank all of my colleagues at the Division of Fluid Dynamics. It has been a true honor working with you and I will miss the creative and friendly atmosphere which you are all a part of creating. Whatever strange question I have come up with, you have always been there, ready to help me. I will also miss the coffee discussions about flying green cows, the true nature of salty sticks and other issues essential to life.

The Swedish Energy Agency (STEM) is gratefully acknowledged for the financial support and SNIC and UNICC are acknowledged for providing the computational resources used to produce many of the results in this thesis.

Last, but certainly not least, I would like to thank my beloved wife Maria. You are my eternal light, guiding and supporting me, even in times of compact darkness.



# Nomenclature

## *Latin symbols*

$a$	Speed of sound
$a^n$	POD coefficient number $n$
$c_b$	Blending coefficient
$C_f$	Skin friction coefficient
$c_p$	Specific heat capacity at constant pressure
$c_v$	Specific heat capacity at constant specific volume
$e$	Internal energy
$F$	Flux vector
$\mathcal{F}$	Filtered flux vector
$h$	Enthalpy
$k$	Turbulent kinetic energy
$M$	Mach number
$p$	Pressure
$Pr$	Prandtl number
$Q$	Flow variables
$\tilde{Q}$	Filtered flow variables
$q_i$	Heat flux vector
$\vec{q}$	Vector for primitive variables
$R$	Gas constant
$Re$	Reynolds number
$S_{ij}$	Strain rate tensor
$T$	Temperature
$\langle u_i u_j \rangle$	Resolved Reynolds stresses
$u, v, w$	$x$ -, $y$ - and $z$ - velocities, also denoted $u_1, u_2$ and $u_3$
$V$	Cell volume

### *Greek symbols*

$\Delta$	Filter width
$\delta_{99}$	Boundary layer thickness
$\delta_{ij}$	The Kronecker delta
$\Delta t$	Time step
$\Delta x, \Delta y, \Delta z$	Cell length, height and width
$\gamma$	Specific heat ratio
$\lambda$	Eigenvalue
$\mu$	Dynamic viscosity
$\nu$	Kinematic viscosity
$\phi^n$	POD mode number $n$
$\rho$	Density
$\tau_{ij}$	Viscous stress tensor
$\mathcal{O}$	Ordo

### *Subscripts*

$\infty$	Freestream condition
0	Total quantity
$t$	Turbulent quantity

### *Superscripts*

–	Space filtered quantity
$\tilde{\phantom{x}}$	Favre filtered quantity
"	Deviation from Favre averaged value
+	Wall friction units
$SGS$	Subgrid scale quantity

### *Other symbols*

$\langle \rangle$	Filtered in homogeneous directions
-------------------	------------------------------------

### *Conventions*

*Nodes and cells.* The grids, which are structured grids, are built up of nodes. A cell consists of eight nodes, one in each corner. The flow data are represented as averages over these cells.

# Contents

<b>Abstract</b>	<b>iii</b>
<b>List of publications</b>	<b>v</b>
<b>Acknowledgments</b>	<b>vii</b>
<b>Nomenclature</b>	<b>ix</b>
<b>1 Introduction</b>	<b>1</b>
1.1 Motivation . . . . .	1
1.2 Internal transonic flow . . . . .	2
1.3 Large scale shock movement . . . . .	5
1.4 Advantages and limitations of LES . . . . .	7
1.5 Hybrid methods . . . . .	8
<b>2 Large eddy simulation technique</b>	<b>11</b>
2.1 Governing equations . . . . .	11
2.2 Large eddy formulation . . . . .	12
2.2.1 The continuity equation . . . . .	12
2.2.2 The momentum equations . . . . .	13
2.2.3 The energy equation . . . . .	13
2.2.4 Subgrid Models and Constants . . . . .	14
2.3 Space discretization . . . . .	15
2.4 Time stepping . . . . .	17
2.5 Boundary conditions . . . . .	19
<b>3 Shock/boundary layer interaction</b>	<b>21</b>
3.1 A baseline case . . . . .	21
3.2 Search for large scale shock movement . . . . .	23
<b>4 A new subgrid model</b>	<b>27</b>
4.1 Reconstruction of turbulent channel flow . . . . .	27
4.2 Towards higher Reynolds number . . . . .	30
4.2.1 Matching plane location . . . . .	30

4.2.2	Scaling issues . . . . .	31
<b>5</b>	<b>Conclusions and recommendations for future work</b>	<b>33</b>
<b>A</b>	<b>Space discretization</b>	<b>35</b>
A.1	Convective fluxes . . . . .	35
A.2	Diffusive fluxes . . . . .	38
A.3	Extra diffusion for strong shocks . . . . .	39
A.4	Non-reflective boundary conditions . . . . .	40
	<b>Bibliography</b>	<b>41</b>

# Chapter 1

## Introduction

### 1.1 Motivation

Shock wave turbulent boundary layer interactions (SWTBLI) have been studied for many years. These situations commonly arise in turbomachinery, aerospace applications and on the exterior of high speed aircraft. In all these cases, shock wave boundary layer interactions can significantly change the flow and hence the physical load imposed by them. The rapid pressure rise associated with a shock will impose high strain rates in the material of the walls and will decrease the life span of the material, especially in the case of significant shock movement. SWTBLI is an important issue in attempts to predict heat transfer since the heat loads will change dramatically with different shock positions. The performance of the object studied can also be significantly altered if shocks and boundary layer separations do not occur where expected. It is therefore desirable to have reliable and effective prediction tools for SWTBLI. No such tools currently exist, however. Instead, compromises must often be made in performance to ensure dependability.

The experimental material on SWTBLI is vast, but most of it is produced using intrusive methods [1] and only a basic understanding of the phenomenon has been achieved in older experiments [2]. There are newer techniques, of course, such as particle induced velocimetry (PIV) and laser doppler anemometry (LDA), that can give a deeper understanding [3], especially when combined with numerical simulations (see for example [4]).

The bulk of the existing calculations are from Reynolds averaged Navier-Stokes (RANS) computations since the high computational cost has long hindered more advanced calculations. In recent years, large eddy simulations (LES) [5], [6] have been made that show much better agreement with experiments than RANS calculations [7]. This gain in accuracy comes however at a cost that is unacceptable for industrial ap-

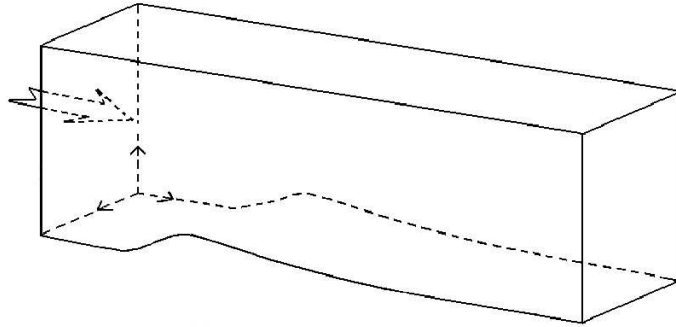


Figure 1.1: Experimental geometry to create transonic flow. The arrow indicates flow direction.

plications. Hence, there is an obvious need to develop numerical models that retain most of the accuracy of LES at a cost not much higher than RANS. This task requires a deep understanding of the modeled phenomena. LES is used in this work to gain greater understanding since LES seems to be the only tool apart from direct numerical simulation (DNS) which gives results that are sufficiently accurate.

## 1.2 Internal transonic flow

Internal transonic flows can be created by several different configurations but nominally two dimensional flows are often chosen since they facilitate studies of more specific phenomena. From an experimental point of view, two dimensional flows are easier to investigate than three dimensional flows but more difficult to realize since so called end-wall effects are often an issue. From a numerical point of view, it is relatively cheap to implement two dimensional flows since the demands on domain size and number of walls that need to be resolved decrease drastically as compared with a three dimensional flow.

The exact geometry used to create the two dimensional flow is often inspired by the applications to wings, turbomachinery and aerospace devices. The geometry used in this work is shown in figure 1.1 and resembles the cut-through profile of a traditional nozzle. The arrow indicates the flow direction. As the subsonic flow reaches the bump it will accelerate. This acceleration can be controlled by the outlet pressure; lower pressure gives stronger acceleration. For some conditions, the acceleration will result in a sonic pocket that is terminated by a shock as sketched in figure 1.2. The domain shown in figure 1.1 is a part of an experimental rig located at the Department of Energy Technology at the Royal Institute of Technology (KTH) in Stockholm. Experiments

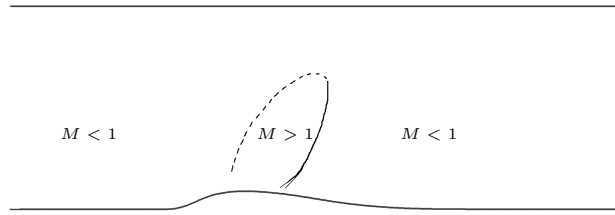


Figure 1.2: Principal sketch of internal transonic flow with a shock.

have been conducted by Oliver Bron and Timmy Sigfrids and the flow conditions in this work are guided by their experiments [8], [9].

There are two boundary layers in the channel, one along the ceiling and one along the bottom wall. The term SWTBLI refers foremost to the interaction between the shock and the lower boundary layer. The incoming boundary layer is often characterized by the incompressible shape factor defined by

$$H = \frac{\delta^*}{\theta} = \frac{\int_0^\infty \left(1 - \frac{u}{u_\infty}\right) dn}{\int_0^\infty \frac{u}{u_\infty} \left(1 - \frac{u}{u_\infty}\right) dn} \quad (1.1)$$

where  $\delta^*$  is the displacement thickness,  $\theta$  is the momentum-loss thickness,  $u$  is the wall parallel velocity and  $n$  is the wall normal direction. The shape factor is also known as the form factor. Its importance can be recognized by the fact that, if the Mach number before the shock and the shape factor of the boundary layer approaching the shock are kept constant, the interaction between the shock and the boundary layer is then almost independent of the Reynolds number [2].

However, it is more or less impossible to actually keep the shape factor constant when changing for example the Reynolds number. As the turbulent boundary layer accelerates at the front of the bump, a relaminarization process starts. The relaminarization begins in the outer parts of the boundary layer and reduces the thickness of the boundary layer [10]. The strength of the relaminarization process can for example be described by the acceleration parameter

$$K = \frac{\nu}{u_\infty^2} \frac{du_\infty}{ds} \quad (1.2)$$

given by Jones and Launder [11], where  $s$  is the streamwise direction. As can be seen,  $K$  is directly proportional to the kinematic viscosity,

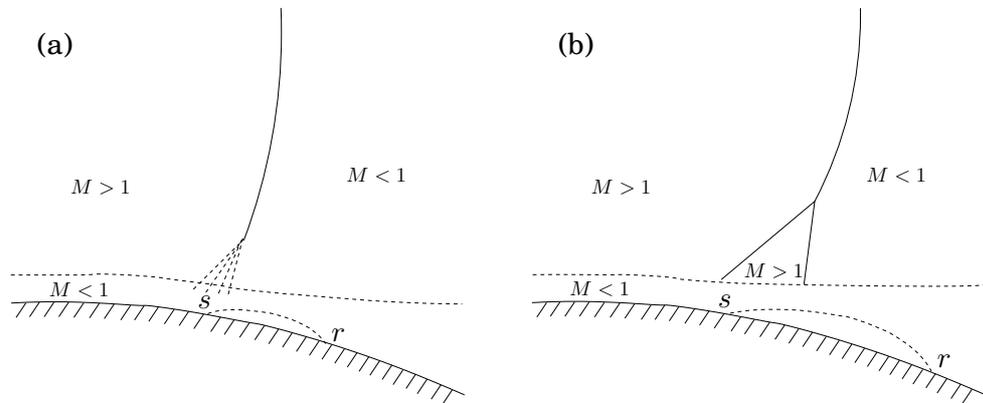


Figure 1.3: a) Shock foot with compression fan. b) Lambda shock pattern.  $s$  and  $r$  are the mean separation and reattachment points respectively.

and the most common way to change the Reynolds number is, at least in computational fluid dynamics, to change the viscosity.

The information transport by pressure waves traveling upstream through the subsonic boundary layer is sometimes referred to as elliptic leakage. Due to this elliptic leakage, the adverse pressure gradient at the shock will influence the boundary layer some distance upstream of the shock. This distance is known as the interaction length and scales with  $\delta^*$  for a given shape factor but increases with increasing Reynolds number based on  $\delta_{99}$  [2]. If the shock is strong enough, the adverse pressure gradient will cause the turbulent boundary layer to separate. The stronger the shock is, i. e. the higher the Mach number before the shock is, the stronger the separation will be. Strong separation is identified by high Reynolds stresses, a large degree of anisotropy, large flow structures behind the shock and a high probability of back-flow in the separated region. The innermost part of the shock itself, the so called shock foot, will also change character with the shock strength. For weak and moderately strong shocks, there will be a compression fan that converges to the shock. For stronger shocks, the compression fan is insufficient to raise the pressure and deviate the flow direction as much as required, and the fan is then replaced by two shocks in a so called lambda shock pattern. Both cases are sketched in figure 1.3.

The aforementioned end-wall effects are possible to avoid by considering an axisymmetric configuration instead of a nominally two dimensional one [12]. The geometry of this work was initially intended as a pre-study geometry. The main geometry was a three dimensional bump to which there is no axisymmetric counterpart. There is almost no quantitative experimental data available from any of the geometries

and the 3D geometry was out of the question in lack of extensive validation data.

### 1.3 Large scale shock movement

A flow case with SWTBLI can also feature so called large scale shock movement. This means that the shock moves back and forth over a distance comparable with the boundary layer thickness or the interaction length. Furthermore, the frequency of the movement is often very low compared to any number of  $U/L$  that can be constructed of a velocity scale  $U$  and a length scale  $L$  in the vicinity of the shock. The movement of the shock can of course be achieved for example by a fluctuating outlet pressure, but it is also possible to get what is believed to be a self excited movement. The latter is interesting because the exact prerequisites for self excitement are not known. Movement seems however to be present only in connection with strong separation of the boundary layer [2]. Since strong separation is often achieved by strong shocks, the lambda shock formation is commonly observed when the shock features large scale shock movement [9], [13]. Neither is it known how the self excited shock movement is created nor what parts of the flow or flow structures that determine the frequency of the shock movement. While many experiments and calculations have been done that feature large scale shock movement [2], [8], [13], [14], there have also been simulations of seemingly similar flows but where the shock is steady. The latter can be seen in [5] and in chapter 3 here.

The connection between flow structures and unsteady shock movement has chiefly been investigated for supersonic flow in a compression ramp such as the one depicted in figure 1.4. Thomas et al. [15] related the shock movement to the frequency of wall pressure fluctuations in the separated region and to the turn-over time of the separation bubble. There are significant differences between the transonic case and the supersonic compression ramp. In the supersonic case, the separation bubble is 'trapped' between the shock and the compression ramp, whereas transonic flows feature not one but several separation bubbles. Thus, no single turnover time can be computed for the transonic cases. On the other hand, several investigations of supersonic compression ramp flow have indicated the bursting frequency of the incoming boundary layer to be the frequency of the shock movement. See for example [16] and [17]. To detect possible burst events in the incoming boundary layer Wu and Martin [16] applied an indicator function at a distance of  $0.5\delta_{99}$  from the

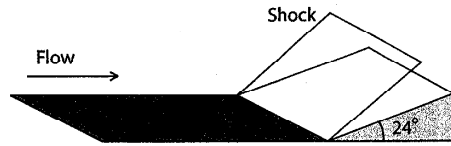


Figure 1.4: A supersonic compression ramp with  $24^\circ$  deflection angle. Sketch taken from [16].

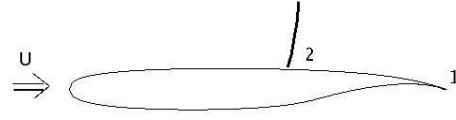


Figure 1.5: Whitcomb supercritical airfoil. Flow from left to right.  $U$  is the free stream velocity. 2 indicates the separation region behind the shock.

wall. The indicator function,  $I_M$ , was defined by

$$I_M = \begin{cases} 1 & \text{if } M > \langle M \rangle + \sigma_M \\ -1 & \text{if } M < \langle M \rangle - \sigma_M \\ 0 & \text{otherwise} \end{cases} \quad (1.3)$$

where  $\sigma_M$  is the standard deviation of the Mach number distribution. They found that bursts and shock movement had a main frequency of  $0.14U_\infty/\delta$ .

The most common configuration for studying transonic SWTBLI is the supercritical airfoil such as the one shown in figure 1.5. Shock movement in such a configuration is known as the “buffeting phenomenon”. Recent numerical investigations [18],[19] support the theory proposed by Lee [20]. Lee suggested that the separation (point 2 in figure 1.5) causes large scale structures that are convected downstream. As these structures reach the trailing edge (point 1 in figure 1.5) they interact with the flow coming from underneath the airfoil. This interaction causes radiation of acoustic waves which in turn propagate upstream to the shock leading to a feedback mechanism. Since geometries for internal transonic flows do not have trailing edges, no feedback mechanism such as that in the airfoil case can be present. It is however interesting to note that it is upstream traveling waves from far downstream of the shock that determine the large scale shock movement rather than bursting events in the incoming boundary layer or direct interaction between the shock and separation bubbles directly behind the shock.

Handa and Masuda [14] made experiments and quasi one-dimensional computations of a transonic diffuser. They investigated two different maximal Mach numbers before the shock (1.26 and 1.48) and the shocks reached from the lower boundary layer to the boundary layer in the ceiling. They suggest that, as pressure waves generated by the turbulence in the separated region hit the roof, new pressure waves are created that travel upstream along the roof and move the shock as they reach

it.

Much of this thesis is concerned with the question of large scale shock movement and its possible connection with SWTBLI.

## 1.4 Advantages and limitations of LES

This section describes briefly the advantages of LES over unsteady RANS (URANS) which is the main alternative to LES for transonic flows.

RANS models are almost always derived considering time averaged cases. Assumptions, constants and closure relations are all calibrated for steady flows. This can be seen in for example [21] and [22]. Still the models are used in an unsteady mode which is valid only if there is a time separation between the resolved and modeled scales. Typical for two equation RANS models used in unsteady mode is that the turbulent length scale is severely overpredicted [23] and Dolling [1] pointed out that the major reason that URANS cannot be used in transonic flow is that it fails to predict the flowfield unsteadiness.

It is possible to try to mend some of the deficiencies of RANS models by *ad hoc* adjustments. Sinha et al. [24] tried to modify three different RANS models to better predict the separation point in a compression ramp flow. They succeeded, but the process made the prediction of the reattachment point worse for two out of three models. Along the same line, Thivet et al. [25] applied realizability constraints on the  $k-\omega$  RANS model in an attempt to predict heat transfer in crossing-shock-wave/boundary-layer interactions. Their results improved compared to the original formulation, but “not sufficiently to meet the experimental data”. These examples demonstrate that the details of solutions obtained by URANS simulations cannot be trusted since there are no guarantees that the underlying assumptions are compatible with the current flow. More on the deficiencies of RANS for SWTBLI can be found in [7].

The idea in LES is to model only the smallest scales of turbulence, i. e. the highest wave numbers of the turbulent spectrum. The smallest structures are assumed to be locally isotropic and are thereby easier to model. Every scale of the flow down to the scales of the initial subrange must then be resolved. This makes the demands on resolution much higher than in RANS. See for example [26] for more on basic principles of LES. The assumption that the turbulent spectrum has an inertial subrange is much more seldom violated than assumptions made in RANS models. There are however some parts of the flow where the smallest scales are not isotropic. The buffer zone and viscous sublayer of boundary layers are two of them, and there, the turbulence must be resolved to a much higher degree than in other parts of the flows. This

makes the number of nodes needed for LES of wall bounded flows increase at least like  $Re^{1.8}$  [27]. The same is true for the turbulence in separated regions of SWTBLI [1]. The severe demands on resolution is of course the biggest hinder for LES. As noted by Knight et al. [7], very few large eddy simulations are carried out at Reynolds number corresponding to those of experiments.

The numerical scheme will have stronger impact on the results in LES than in RANS since more of the turbulence is resolved with the former method. A study of the impact of truncation and aliasing errors is presented by Kravchenko and Moin [28]. The most extreme example of coupling between the subgrid model and the numerical scheme is monotone integrated LES (MILES) where the numerical scheme is chosen to incorporate the effects of the subgrid model. See for example Urbin and Knight [29] and Moroianu [13] for examples of MILES for compressible flows.

LES will, if care is taken to ensure that the flow is well resolved and an accurate numerical scheme is used, give results far more accurate than RANS [7] and sometimes comparable to filtered DNS [30]. The results are however not always perfect. Garnier et al. presented LES of Shock/Boundary-Layer Interaction [6]. First order statistics was in very good agreement with experiments, but not all of the turbulent stresses were. Another Achilles heal is heat transfer which is better predicted by LES than by RANS, but still far from well predicted [7]. In general, there are no guarantees that LES will give better predictions than a special RANS model for a specific flow case. But in almost all benchmark cases, LES has proved to give results that are at least as good as the best results obtained by any RANS model [31].

## 1.5 Hybrid methods

The calculations discussed in chapter 3 are computationally very heavy. Even with 20 processors, they each took between one and three months to complete. Such long times are of course not acceptable in industrial applications and demonstrate that LES is a far too expensive method for any practical use outside the academic world. The high cost of LES is caused by the region close to solid wall since there is no LES model that is suitable for modeling the highly anisotropic flow there. Instead of modeling the turbulence, it must be resolved and hence the demands on resolution approaches those of DNS.

A common technique is to use one computational method close to the wall and another in the outer region. These so called hybrid methods, or zonal methods, have been explored for example by Davidson and Peng [32], Hamba [33] and Tucker and Davidson [34], all of whom used

some RANS model close to the wall up to some matching plane and LES outside that plane. The argument in favor of these methods working is that the LES and the RANS formulations of the Navier-Stokes equations are the same when the stress terms are expressed in terms of the turbulent viscosity,  $\nu_t$ . Hence any model can be used for  $\nu_t$ . LES is used away from walls since it provides good accuracy at a reasonable computational cost everywhere except for regions close to walls. Close to walls, RANS is currently the only feasible method for calculations at high Reynolds number and is thus applied there.

There are however conceptual problems in this approach. For plane channel flow, hybrid methods give a sudden increase in the mean streamwise velocity somewhere outside the matching plane [32]. The reason is that RANS gives much higher values of  $\nu_t$  and will therefore affect a much larger part of the turbulent spectrum while LES has levels of  $\nu_t$  that damp only the smallest resolved scales. This will manifest itself as a jump in resolved turbulent scales at the matching plane, as demonstrated in [35].

Some remedies have been suggested. Tucker and Davidson [34] used a one-equation  $k-l$  model in both the RANS and LES regions, and the regions differed in how the filter length scale was chosen. The results for plane channel flow improved when the transition from RANS to LES was made in a smooth manner instead of abruptly changing the filter length scale definition at the matching plane. Several authors have used forcing at the matching plane to reintroduce resolved LES scales from modeled RANS scales. See for example [36], [35], [37] and [38]. Hybrid methods with forcing produce good mean velocity profiles for plane channel flows, but the forcing conditions are rather arbitrary. This is to some extent due to the problem pointed out by Temmerman et al. [39]: resolved turbulence is transported from the LES region into the RANS region, which responds by increasing the turbulent viscosity and thus diminishing the effect of the forcing. This is however not always the case. In the work of Davidson and Billson [37], forcing resulted in a lower value of  $\nu_t$ .

An alternative approach to the problem at the matching plane is given by Hamba [33]. The value of  $\nu_t$  on the RANS side of the matching plane is much higher than on the LES side. To obtain the same level of  $\nu_t$  on the LES side, the filter width must be increased by approximately a factor 5, depending on the exact location of the matching plane. However, the filter operator described in equation (2.8) and the spatial derivatives in the Navier-Stokes equations (equation (2.1)) do not commute in the mathematical sense but do so only to a second-order approximation in terms of the spatial derivative of the filter [40]. Hence, this rapid change in filter width will give rise to serious errors unless accounted for in some way. Hamba adopted a scheme with addi-

tional filtering of the data on the LES side of the matching plane and obtained an improvement for computations of plane channel flow.

Since none of the suggested remedies works without a substantial amount of *ad hoc* adjustment, either the RANS method or the LES method must be replaced. Since the main objective is to be able to make LES without completely resolving the boundary layer, it would be directly counterproductive to remove the LES part. It is therefore the RANS model that is discarded and replaced. Some initial work on this is presented for incompressible flow in chapter 4.

## Chapter 2

# Large eddy simulation technique

### 2.1 Governing equations

The solver for the Navier-Stokes equations is based on the G3D series of codes developed by Lars-Erik Eriksson [41]. The conservative forms of the continuity, momentum and energy equations governing viscous compressible flow, solved by the code, can be written in the form:

$$\frac{\partial}{\partial t}Q + \frac{\partial}{\partial x_i}(F_i - F_{vi}) = 0 \quad (2.1)$$

where

$$Q = \begin{bmatrix} \rho \\ \rho u_1 \\ \rho u_2 \\ \rho u_3 \\ \rho e_0 \end{bmatrix} \quad F_i = \begin{bmatrix} \rho u_i \\ \rho u_1 u_i + p \delta_{1i} \\ \rho u_2 u_i + p \delta_{2i} \\ \rho u_3 u_i + p \delta_{3i} \\ \rho h_0 u_i \end{bmatrix} \quad F_{vi} = \begin{bmatrix} 0 \\ \tau_{1i} \\ \tau_{2i} \\ \tau_{3i} \\ \tau_{ji} u_j - q_i \end{bmatrix}$$

where in turn

$$\tau_{ij} = -\frac{2}{3}\mu \frac{\partial u_m}{\partial x_m} \delta_{ij} + \mu \left( \frac{\partial u_i}{\partial x_j} + \frac{\partial u_j}{\partial x_i} \right) \quad (2.2)$$

$$q_i = -\frac{\mu c_p}{Pr} \frac{\partial T}{\partial x_i} \quad (2.3)$$

To close the equation system, calorically perfect gas is assumed, i.e. the following relations can be used

$$p = \rho RT \quad (2.4)$$

$$e = c_v T \quad (2.5)$$

$$h = c_p T \quad (2.6)$$

$$c_v = c_p - R \quad (2.7)$$

$c_p$  is a constant and  $\mu$  is the dynamic viscosity.  $R$  is the ideal gas constant.

## 2.2 Large eddy formulation

A filtered quantity,  $\bar{\Phi}$ , is obtained from the unfiltered quantity,  $\Phi$ , by the integral operation

$$\bar{\Phi}(x_i, t) = \int_{\mathcal{R}^3} G(r_i, x_i) \Phi(x_i - r_i, t) dr_1 dr_2 dr_3 \quad (2.8)$$

For each  $x_i$ , the filter function  $G(r_i, x_i)$  has a maximum at  $r_i = 0$  and  $G(r_i, x_i) \leq G(0, x_i) \forall r_i \in \mathcal{R}^3$ . Furthermore,  $G(r_i, x_i)$  is normalized so that

$$\int_{\mathcal{R}^3} G(r_i, x_i) dr_1 dr_2 dr_3 = 1 \forall x_i \in \Omega \quad (2.9)$$

where  $\Omega$  is the computational domain. Hence, for a specific  $x_i$ ,  $\bar{\Phi}(x_i, t)$  will be a weighted average of all values within some volume centered at  $x_i$ . The size of the volume can be represented by some length scale  $\Delta$  which is called the filter width.

The large eddy formulation is obtained by applying the filter operation to the governing equations. The result, however, is often written using the Favre notation since the results then look very similar to the unfiltered equations. The Favre averaged quantity,  $\tilde{\Phi}$ , is related to  $\bar{\Phi}$  by

$$\tilde{\Phi} = \frac{\rho \bar{\Phi}}{\bar{\rho}} \quad (2.10)$$

and to the unfiltered quantity,  $\Phi$ , by

$$\Phi = \tilde{\Phi} + \Phi'' \quad (2.11)$$

$\tilde{\Phi}$  is the resolved part of  $\Phi$  and  $\Phi''$  the unresolved part. Since  $G(r_i, x_i)$  is often related to the computational grid in some way,  $\Phi''$  is called the subgrid fluctuations of  $\Phi$ .

The modeling approach used in the code is very similar to the one described by Erlebacher et.al [42] which gives details about the modeling assumptions.

### 2.2.1 The continuity equation

Upon filtering, the continuity equation becomes

$$\frac{\partial \bar{\rho}}{\partial t} + \frac{\partial(\bar{\rho} \tilde{u}_i)}{\partial x_i} = 0 \quad (2.12)$$

which needs no modeling.

### 2.2.2 The momentum equations

Applying the space filter to the momentum equations gives

$$\frac{\partial(\bar{\rho}\tilde{u}_i)}{\partial t} + \frac{\partial(\bar{\rho}\tilde{u}_i\tilde{u}_j)}{\partial x_j} = -\frac{\partial\bar{p}}{\partial x_i} + \frac{\partial\bar{\tau}_{ij}}{\partial x_j} + \frac{\partial\tau_{ij}^{SGS}}{\partial x_j} \quad (2.13)$$

Only the last term on the right hand side in equation (2.13) needs modeling. It can be written as:

$$\frac{\partial\tau_{ij}^{SGS}}{\partial x_j} = \frac{\partial}{\partial x_j} \left( -\bar{\rho}(\widetilde{\tilde{u}_i\tilde{u}_j} - \tilde{u}_i\tilde{u}_j) - \bar{\rho}(\widetilde{\tilde{u}_i u_j''} + \widetilde{u_i''\tilde{u}_j}) - \bar{\rho}\widetilde{u_i''u_j''} \right) \quad (2.14)$$

$\tau_{ij}^{SGS}$  is the subgrid stress tensor and is modeled in the code by

$$\tau_{ij}^{SGS} = \mu_t \left( \tilde{S}_{ij} - \frac{1}{3}\tilde{S}_{mm}\delta_{ij} \right) - \frac{2}{3}\bar{\rho}k^{SGS}\delta_{ij} \quad (2.15)$$

where  $\tilde{S}_{ij}$  is the Favre filtered strain rate tensor given by

$$\tilde{S}_{ij} = \frac{1}{2} \left( \frac{\partial\tilde{u}_i}{\partial x_j} + \frac{\partial\tilde{u}_j}{\partial x_i} \right) \quad (2.16)$$

The turbulent viscosity,  $\mu_t$ , and the subgrid kinetic energy,  $k^{SGS}$ , depend on the subgrid model (see section 2.2.4).

### 2.2.3 The energy equation

When the energy equation is filtered, the following expression is obtained:

$$\frac{\partial(\bar{\rho}\tilde{e}_0)}{\partial t} + \frac{\partial(\bar{\rho}\tilde{h}_0\tilde{u}_i)}{\partial x_i} = -\frac{\partial\bar{q}_i}{\partial x_i} + \frac{\partial(\overline{\tau_{ij}u_j})}{\partial x_i} + \frac{\partial\Phi_i}{\partial x_i} \quad (2.17)$$

There are two terms that need modeling in equation (2.17), the derivatives of  $\overline{\tau_{ij}u_j}$  and the last term on the right hand side which, written out, is

$$\begin{aligned} \frac{\partial\Phi_i}{\partial x_i} = & \frac{\partial}{\partial x_i} \left( q_i^{SGS} + \bar{\rho}\widetilde{u_k u_k'' u_j''} + \frac{1}{2}\bar{\rho}\widetilde{u_k \tilde{u}_k u_j''} + \frac{1}{2}\bar{\rho}\widetilde{u_k'' u_k'' u_j''} \right. \\ & + \bar{\rho} \left( \frac{1}{2} \left( \widetilde{\tilde{u}_k \tilde{u}_k \tilde{u}_j} - \widetilde{\tilde{u}_k \tilde{u}_k \tilde{u}_j} \right) + \left( \widetilde{\tilde{u}_k u_k'' \tilde{u}_j} - \widetilde{\tilde{u}_k u_k'' \tilde{u}_j} \right) + \right. \\ & \left. \left. \frac{1}{2} \left( \widetilde{u_k'' u_k'' \tilde{u}_j} - \widetilde{u_k'' u_k'' \tilde{u}_j} \right) + \left( \widetilde{\tilde{u}_k u_k'' u_j''} - \widetilde{\tilde{u}_k u_k'' u_j''} \right) \right) \right) \end{aligned} \quad (2.18)$$

where

$$q_i^{SGS} = \bar{\rho}c_p \left( \widetilde{\tilde{T}u_i} - \tilde{T}\tilde{u}_i + \widetilde{T''\tilde{u}_i} + \widetilde{\tilde{T}u_i''} + \widetilde{T''u_i''} \right) \quad (2.19)$$

represents the subgrid heat fluxes and is modeled using

$$q_i^{SGS} = -c_p \frac{\mu_t}{Pr_T} \frac{\partial \tilde{T}}{\partial x_i} \quad (2.20)$$

$Pr_T$  is the turbulent Prandtl number which is given by the user.  $\widetilde{u_k'' u_j''}$  is modeled with  $\tau_{kj}^{SGS}$ . The differences in triple correlation and the term  $\widetilde{\bar{\rho} u_k'' u_k'' u_j''}$  can be modeled, but has in the work by Larsson [43] been found to have negligible effects in RANS. Since the subgrid fluctuations in LES are considerably smaller than in RANS, the terms are neglected here as well. The term  $\widetilde{\bar{\rho} \tilde{u}_k \tilde{u}_k u_j''}$  is discarded by the same arguments. Finally,  $\overline{\tau_{ij} u_j}$  in equation (2.17) is replaced by  $\bar{\tau}_{ij} \tilde{u}_j$ .

## 2.2.4 Subgrid Models and Constants

Two different subgrid models are used.

The first subgrid model is a compressible version of the Smagorinsky model [42] with a fixed filter width. In this Smagorinsky model  $\mu_t$  and  $k^{SGS}$  are given by

$$\mu_t = C_R \bar{\rho} \Delta^2 \sqrt{\tilde{S}_{mn} \tilde{S}_{mn}} \quad (2.21)$$

$$k^{SGS} = C_I \Delta^2 \tilde{S}_{mn} \tilde{S}_{mn} \quad (2.22)$$

Constants  $C_R$  and  $C_I$  were set to 0.012 and 0.0066 respectively [44]. The dynamic viscosity is set to a constant value (see chapter 3). The filter width is set to the average value of  $(\Delta x \Delta y \Delta z)^{1/3}$  for the inner part of the boundary layer where the subgrid model has its strongest influence.

A LES should be tested for its dependence on the subgrid model. The Smagorinsky subgrid model is not always accurate enough, but the flaws are difficult to correct since its length scale needs to be damped out close to a wall and the damping functions commonly used, for example van Driest damping [45], do not work in separated regions. Thus a modified version of the WALE model, developed by Nicoud and Ducros [46], is tested.

The original model is developed for incompressible flow and it thus gives only  $\mu_t$ :

$$\mu_t = \bar{\rho} (C_w \Delta)^2 \frac{\left( S_{ij}^d S_{ij}^d \right)^{3/2}}{\left( \tilde{S}_{ij} \tilde{S}_{ij} \right)^{5/2} + \left( S_{ij}^d S_{ij}^d \right)^{5/4}} \quad (2.23)$$

where  $C_w = 0.3$  and

$$S_{ij}^d = \frac{1}{2} \left( \frac{\partial \tilde{u}_i}{\partial x_l} \frac{\partial \tilde{u}_l}{\partial x_j} + \frac{\partial \tilde{u}_j}{\partial x_l} \frac{\partial \tilde{u}_l}{\partial x_i} \right) - \frac{1}{3} \frac{\partial \tilde{u}_m}{\partial x_l} \frac{\partial \tilde{u}_l}{\partial x_m} \delta_{ij} \quad (2.24)$$

The modification is to use the relation between  $\mu_t$  and  $k^{SGS}$  in equation (2.21) and (2.22) to rewrite equation (2.15) as

$$\tau_{ij}^{SGS} = 2\mu_t \left( \tilde{S}_{ij} - \frac{1}{3} \tilde{S}_{mm} \delta_{ij} \right) - \frac{2}{3} \frac{C'_I}{\bar{\rho}} \left( \frac{\mu_t}{\Delta} \right)^2 \delta_{ij} \quad (2.25)$$

Using the the coefficients from the Smagorinsky model,  $C'_I$  is found to be 45.8, which is also used in the modified WALE model. To make the stresses realizable, their diagonal entries were forced to be non-positive. Further improvement is achieved by changing the filter to be given by  $(\Delta x \Delta y \Delta z)^{1/3}$ , i. e. to a function of the grid, and the dynamic viscosity to follow Sutherland's law [47].

There is evidence that SGS models with only one length scale are not functional in areas with large anisotropy, for example in separated regions [1]. However, this type of problem can be remedied if the grid is fine enough in the critical regions.

## 2.3 Space discretization

For spatial discretization, one scheme is used for the inviscid terms and another for the viscous terms. The filtered and modeled version of equation (2.1) can be written in the form

$$\frac{\partial \mathcal{Q}}{\partial t} + \frac{\partial}{\partial x_i} (\mathcal{F}_i - \mathcal{F}_{vi}) = 0 \quad (2.26)$$

where

$$\mathcal{Q} = \begin{bmatrix} \bar{\rho} \\ \frac{\bar{\rho} u_1}{\rho} \\ \frac{\bar{\rho} u_2}{\rho} \\ \frac{\bar{\rho} u_3}{\rho} \\ \frac{\bar{\rho} e_0}{\rho} \end{bmatrix}$$

$\mathcal{F}_i$  and  $\mathcal{F}_{vi}$  can be identified as the filtered and modeled counterparts of the inviscid and viscous parts of the total flux and are also known as the convective and the diffusive fluxes. Equation (2.26) is discretized on a structured non-orthogonal mesh using the Finite Volume Method (FVM). Integrating equation (2.26) over some arbitrary volume,  $\Omega$ , gives

$$\int_{\Omega} \frac{\partial \mathcal{Q}}{\partial t} dV + \int_{\Omega} \frac{\partial}{\partial x_i} (\mathcal{F}_i - \mathcal{F}_{vi}) dV = 0 \quad (2.27)$$

Taking  $\Omega$  to be a cell in the grid and introducing  $\mathcal{S}_j = n_j S$  as the face area normal vector and  $\bar{\mathcal{Q}}$  as the cell average of  $\mathcal{Q}$  over  $\Omega$ , the Gauss theorem can be used to rewrite equation (2.27) as

$$\frac{\partial \bar{\mathcal{Q}}}{\partial t} V + \int_{\partial \Omega} (\mathcal{F}_i - \mathcal{F}_{vi}) d\mathcal{S}_i = 0 \quad (2.28)$$

Since the code uses implicit filtering, i. e. the filter is a box filter of grid cell size,  $\overline{\mathcal{Q}} = \mathcal{Q}$  and the bar notation will be dropped from here on. The integral of the fluxes is approximated by

$$\int_{\partial\Omega} (\mathcal{F}_i - \mathcal{F}_{vi}) dS_j = \sum_{k=1}^{\text{all faces}} (\mathcal{F}_i^k - \mathcal{F}_{vi}^k) \cdot \mathcal{S}_i^k \quad (2.29)$$

where  $\mathcal{F}_i^k$  and  $\mathcal{F}_{vi}^k$  are the cell face averages of the convective and diffusive fluxes respectively and  $\mathcal{S}_i^k$  is the area of the cell faces. In total, the finite volume formulation of equation (2.26) is

$$\frac{\partial \mathcal{Q}}{\partial t} V + \sum_{k=1}^{\text{all faces}} (\mathcal{F}_i^k - \mathcal{F}_{vi}^k) \cdot \mathcal{S}_i^k = 0 \quad (2.30)$$

The inviscid fluxes are discretized in space using a fourth order central scheme to which is added a small amount of upwinding. The upwinding is a third difference multiplied with a user defined constant and applied to the characteristic variables, which are in turn evaluated using a planar wave assumption. This construction makes the space discretization of the inviscid fluxes third order accurate in terms of dissipation, but still makes it fourth order in terms of dispersion.

A second order central scheme is used for the viscous fluxes.

At strong pressure gradients, such as at shocks, extra diffusion is needed to prevent the calculations from diverging. Here a term scaled by the second derivative of the local pressure and the spectral radius of the discretized flux operator is added in the calculations of the inviscid fluxes [48]. The user defined coefficient that guides the level of extra dissipation is set to a level just high enough to prevent divergence.

The discretization schemes and shock handling diffusion are described in detail in appendix A.

The scheme as described in appendix A assumes an uniform Cartesian grid. Stretching and curvature of the grid introduce errors of order

$$\mathcal{O}\left(\frac{\partial^2 \xi_i}{\partial x_j}\right) \quad (2.31)$$

where  $\xi_i$  is the grid of the computational (homogeneous) domain [49]. Of course, this requires that the transformation is second order continuous which has been ensured by using smoothing routines [50] when constructing the meshes. The box filter of grid cell size will also introduce an error when the grid is non-homogeneous since the filter operator and the spatial derivatives do not commute. The leading error term will be of order [40]

$$\mathcal{O}\left(\frac{\partial^2 \Delta}{\partial x_i}\right) \quad (2.32)$$

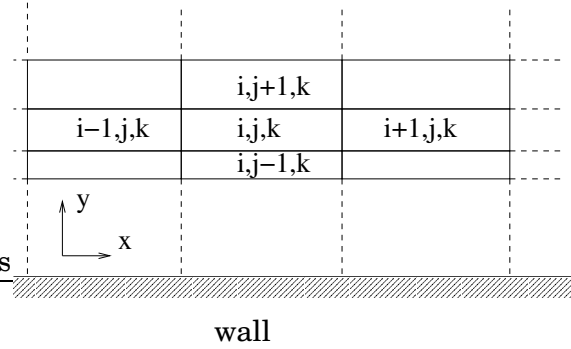


Figure 2.1: Typical cut-through plane of a structured, Cartesian grid used for computations of a wall bounded flow.

This makes it even more important to stretch the grid as little as possible. The maximum stretching of the grids used in this work is in the wall normal direction and is 10 %. The stretching in the streamwise and spanwise directions are negligible.

## 2.4 Time stepping

Time stepping is performed by a three stage, low storage Runge-Kutta method combined with a semi-implicit precondition scheme. The general outline resembles the ordinary use of the Runge-Kutta method, which is as follows. By using the latest known data,  $Q^n$  that is valid for time step  $n$ ,  $\frac{\partial Q}{\partial t}$  is approximated using the methods described hitherto in this chapter. This term is denoted  $(\frac{\partial Q}{\partial t})^n$ . The three stages are then

$$\begin{aligned} Q^* &= Q^n + \Delta t \left( \frac{\partial Q}{\partial t} \right)^n \\ Q^{**} &= \frac{1}{2} \left( Q^n + Q^* + \Delta t \left( \frac{\partial Q}{\partial t} \right)^* \right) \\ Q^{n+1} &= \frac{1}{2} \left( Q^n + Q^* + \Delta t \left( \frac{\partial Q}{\partial t} \right)^{**} \right) \end{aligned} \quad (2.33)$$

where  $\Delta t$  denotes the size of the time step between time step  $n$  and  $n + 1$ . Super scripts  $*$  and  $**$  denote sub-time steps. More on Runge-Kutta schemes can be found in [51].

In the following discussion of the semi-implicit preconditioning, it will be assumed that the grid is Cartesian. If it is not, it can be transformed into a Cartesian one (see for example [52]). All formulations will then apply to the transformed equations instead. This transformation is actually done in the code but will not be described here.

Simulations of instationary flows using a pure explicit time stepping formulation require the same  $\Delta t$  to be used in the whole domain.

Given a discretized solution to the Navier-Stokes equation and a maximal allowed CFL number, the maximum time step for each cell can be calculated from the definition of the CFL number:

$$\begin{aligned} \text{CFL}_{i,j,k} = & |u_{i,j,k}| \frac{\Delta t}{\Delta x_{i,j,k}} + |v_{i,j,k}| \frac{\Delta t}{\Delta y_{i,j,k}} + |w_{i,j,k}| \frac{\Delta t}{\Delta z_{i,j,k}} \\ & + a_{i,j,k} \Delta t \sqrt{\frac{1}{\Delta x_{i,j,k}^2} + \frac{1}{\Delta y_{i,j,k}^2} + \frac{1}{\Delta z_{i,j,k}^2}} \end{aligned} \quad (2.34)$$

where  $a$  is the speed of sound. The indexes refer to the grid as shown in figure 2.1. The cut-through plane of the grid depicted there has very high aspect ratios, i. e.  $\Delta y \ll \Delta x$  and  $\Delta y \ll \Delta z$ , which is typical for the wall proximate region of grids used for computations of wall bounded flows. Due to the no-slip conditions at the walls, the velocities there are typically small; consequently, the CFL number for cells close to walls can be approximated by

$$\text{CFL}_{i,j,k} \approx a_{i,j,k} \Delta t \sqrt{\frac{1}{\Delta y_{i,j,k}^2}} \quad (2.35)$$

This expresses the fact that the maximum allowed time step for cells close to walls is restricted by sound waves in the wall normal direction. Actually, for most structured grids, the global time step will be limited by these wall proximate cells. While these sound waves do not have to be explicitly resolved, their effect must be accounted for. Hence, an idea could be to use an implicit time stepping method close to the wall and another away from it. However, this can be done in an even better way.

Take the first part of equation (2.33) for the cell with indexes  $i, j, k$  and write

$$\left( \frac{dQ_{i,j,k}}{dt} \right)^{\text{expl.}} = \frac{Q_{i,j,k}^* - Q_{i,j,k}^n}{\Delta t} = \left( \frac{dQ}{dt} \right)_{i,j,k}^n \quad (2.36)$$

The corresponding implicit formulation would be

$$\left( \frac{dQ_{i,j,k}}{dt} \right)^{\text{impl.}} = \frac{Q_{i,j,k}^* - Q_{i,j,k}^n}{\Delta t} = \left( \frac{dQ}{dt} \right)_{i,j,k}^* \quad (2.37)$$

where the rightmost term is then of course unknown. Now, equation (2.37) can be Taylor expanded in time. Using the facts that  $\Delta y \ll \Delta x$  and  $\Delta y \ll \Delta z$  close to walls, the following expression can be derived:

$$\begin{aligned} \left( \frac{dQ_{i,j,k}}{dt} \right)^{\text{impl.}} + \frac{\Delta t}{2\Delta y_{i,j,k}} \left( \frac{\partial \mathcal{F}_2^t}{\partial Q} \right)_{i,j+1,k}^n \left( \frac{dQ_{i,j+1,k}}{dt} \right)^{\text{impl.}} - \\ \frac{\Delta t}{2\Delta y_{i,j,k}} \left( \frac{\partial \mathcal{F}_2^t}{\partial Q} \right)_{i,j-1,k}^n \left( \frac{dQ_{i,j-1,k}}{dt} \right)^{\text{impl.}} = \left( \frac{dQ_{i,j,k}}{dt} \right)^{\text{expl.}} \end{aligned} \quad (2.38)$$

where  $\mathcal{F}_2^t = \mathcal{F}_2 - \mathcal{F}_{v2}$ . Equation (2.38) couples cells only in the wall normal direction and can be applied to columns of cells from the wall and out to some  $j_{max}$  where the relations  $\Delta y \ll \Delta x$  and  $\Delta y \ll \Delta z$  are no longer valid.

After the system given by equation (2.38) is solved for each column of cells at walls, equation (2.37) is used for the pre-conditioned cells and equation (2.36) for all the other cells to obtain  $\mathcal{Q}^*$ . The method is repeated for each stage in the Runge-Kutta method.

The usage of equation (2.38) is shown in paper I included in this thesis to be equivalent to making one iteration using Newton-Raphson's method for the  $y$ -direction. Paper I also presents a validation of the method for flat plate boundary layer flow with a slight adverse pressure gradient. The inlet Mach number is equal to 0.7 and  $Re_\tau = 632$ , also at the inlet. Each cell that is treated by the precondition scheme requires six times more computational time than cells to which the preconditioning is not applied. The amount of time saved using this scheme is hence dependent on how large a part of the grid cells lies close to a wall. In a transonic case like those described in section 1.2, the scheme allows five times longer time steps and saves about 60 % of the time that would be required if the fully explicit scheme was used.

The details of the implementation of the semi-implicit preconditioning (also given in paper I) are chosen to retain accuracy, not to maximize efficiency. There are several possibilities for saving even more computational time but no such options were tested.

## 2.5 Boundary conditions

The discretization scheme used for the convective fluxes can be reformulated as a so called non-reflective boundary condition. This is described in detail in section A.4 in the appendix. As the name suggests, such a boundary condition does not reflect waves reaching the boundary. This is strictly true only for plane waves approaching the boundary aligned with the boundary normal direction. Waves that are not aligned with the boundary normal will, by this method, be misinterpreted as a plane wave, resulting in the wave being partially deflected. The drawback of this boundary condition is that it requires five independent properties to be specified at the boundary. It is hence suitable for inlet boundary conditions but not for outlet boundaries where only a minimum of variables should be specified. Too many specifications prevent a natural development of the flow in the domain.

A very good way to handle an outlet boundary is to add a buffer zone, i. e. an extension of the domain where the dissipation is drastically increased. Waves that do not dissipate as they approach the outlet bound-

ary will then definitely dissipate before they reach out of the buffer zone back into the original computational domain. A buffer zone was implemented by for example Andersson [53] and Bogey and Bailly [54].

A buffer zone is however computationally extremely expensive. It often increases the number of computational nodes by at least 25 %. To save computational time, a simpler boundary condition is applied to the outlet boundary. The condition uses zeroth order extrapolation for all variables but the static pressure, which is set to a fixed value. Such a boundary condition is totally reflective in terms of acoustic waves giving artificial pressure fluctuations of the order of 100  $Pa$ . Hence, this simple method is not suitable for acoustic computations but is accurate enough for most other computations.

## Chapter 3

# Shock/boundary layer interaction

With the semi-implicit preconditioner, calculations of transonic flows take a little less than half the time otherwise necessary. This enables thorough investigation of a transonic flow over a bump.

The computational domain is a numerical model of a part of an experimental test rig located at the Department of Energy Technology, KTH. The experimental test section shown in figure 1.1 is  $0.44\text{ m}$  long,  $0.10\text{ m}$  wide and  $0.12\text{ m}$  high. The computational domain consists of this test section but has been shortened by  $0.08\text{ m}$  and translational periodicity was assumed in the spanwise direction for a width less than that of the test section. Furthermore, the ceiling has been replaced by a symmetry plane.

The dynamic viscosity has been increased by a factor of 11 compared to the experiments. It is far too costly in terms of computational resources to make an LES of the flow with the correct Reynolds number. It is better to make well resolved large eddy simulations of the case at a reduced Reynolds number than to make poor simulations at the correct Reynolds number.

The investigation of this flow is described in detail in papers *II* and *III* included in this thesis. Only the most important results are given here.

### 3.1 A baseline case

A flow case for which measurements showed large scale shock movement is simulated. A Mach number contour of an average flow field is shown in figure 3.1. Several simulations are made to ensure grid convergence and that the results are not heavily dependent on the subgrid model. Figure 3.1 is produced using a  $4\text{ cm}$  wide domain, and the modi-

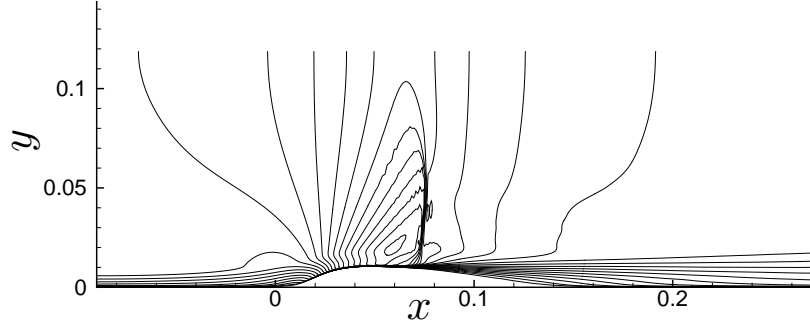


Figure 3.1: Mach number contour plot for transonic flow over a bump. The inlet free stream Mach number is 0.7 and the maximum Mach number before the shock is 1.27. The contour level difference is 0.05.

fied WALE model is used as the subgrid model. Special care is taken to ensure the inlet boundary layer at  $x = -0.09 m$  to be physically correct. The mean profiles are taken from measurements made by Sigfrids [9]. Fluctuations from DNS of fully developed channel flow is rescaled according to measurements made by Johansson and Castillo [55].

The results have been compared with the few experimental data available and show satisfying agreement.

Figure 3.2 shows the probability of backflow along the bottom wall and figure 3.3 shows the maximum of the resolved Reynolds stresses.

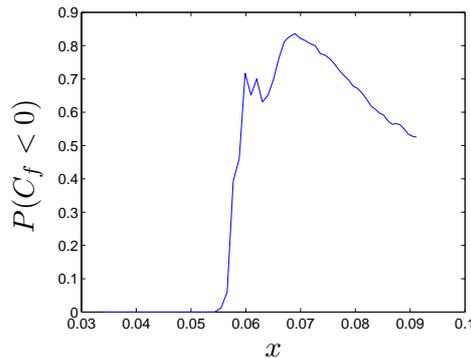


Figure 3.2: The probability for  $C_f$  to be less than zero as a function of the streamwise position.

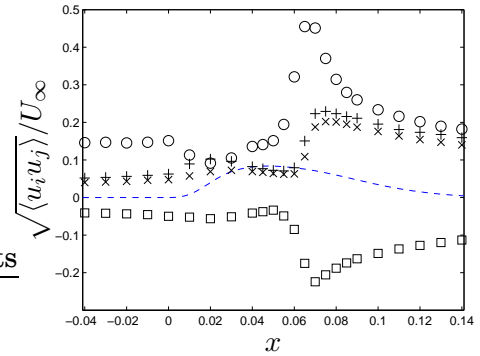


Figure 3.3: Normalized maximum values of the Reynolds stresses.  $\circ = \sqrt{\langle uu \rangle}/U_\infty$ ;  $\times = \sqrt{\langle vv \rangle}/U_\infty$ ;  $+$   $= \sqrt{\langle ww \rangle}/U_\infty$ ;  $\square = \sqrt{\langle |uv| \rangle}/U_\infty$  (sign restored).  $---$  is the wall profile.

As can be seen in figure 3.3, the  $\langle uu \rangle$  stresses are amplified by several hundred percent and the stresses become highly anisotropic at the SWTBLI ( $x \approx 0.07 m$ ). Furthermore, visualization and power spectra of two-point correlations in space and time show that large scale flow structures are produced in the separated region. The high probability of backflow, production of large scale flow structures and strong amplification of the Reynolds stresses indicates that the SWTBLI induces a strong separation of the boundary layer.

The shock position was defined as the streamwise position where the streamwise pressure gradient was at its largest. This position was constant in time for all wall normal distances covered by the shock. The existence of large scale flow structures in the separation region and the lack of shock movement suggests that strong shock induced separation is not a necessary condition for large scale shock movement.

Looking at time space correlation of the streamwise velocity directly beneath the shock reveals that the dominating frequencies are  $250 Hz$ ,  $1.2 kHz$ ,  $1.6 kHz$ ,  $2.1 kHz$  and  $2.8 kHz$ . Only the lowest frequency is transported downstream, all other emanate from the separation region. Specifically, the frequency of  $1.2 kHz$  can be found to be a dominating frequency of the separation. Together with the above observations, it can be concluded that direct interaction between the shock and large scale flow structures directly behind the shock is not a triggering event of large scale shock movement.

The indicator function,  $I_M$ , given by equation (1.3) applied to a position  $x = 0.05 m$  and  $0.5\delta_{99}$  from the wall shows that the boundary layer features bursting events with a main frequency of  $0.133U_\infty/\delta_{99}$ . Hence, bursting events in the incoming boundary layer seem not to be able to trigger large scale shock movement.

The lack of large scale shock movement in this baseline case is in disagreement with many experiments of transonic SWTBLI, for example those presented by Bron [8], but in agreement with LES presented by Sandham et al. [5] and experiments presented by Bachalo and Johnson [12].

## 3.2 Search for large scale shock movement

Motivated by several other investigations of SWTBLI, changes were made to the domain configuration and the boundary conditions. In case 1, the symmetry plane was lowered to  $y = 0.08$  to produce a choked flow. Another choked configuration was created by keeping the geometry of the baseline case but lowering the outlet pressure. The important difference between cases 1 and 2 is that the former has a relatively larger mass displacement since the bump covers a larger part of the domain.

Case	Domain height	Outlet pressure	Ceiling
baseline	0.1186 m	103.5 kPa	no
1	0.08 m	103.5 kPa	no
2	0.1186 m	101 kPa	no
3	0.12 m	101 kPa	yes
4	0.12 m	96 kPa	yes

Table 3.1: Summary of the cases.

Two cases in which the ceiling was included were also simulated, one in which the flow was not choked (case 3) and one with choked flow (case 4). The cases are summarized in table 3.1. In all cases, the resolution is the same as in the baseline case for which grid convergence was proved. In cases 3 and 4, the ceiling boundary layer has the same resolution as the baseline case boundary layer has at the inlet, i.e.  $\Delta x^+ \approx 100$ ,  $\Delta z^+ \approx 15$  and  $\Delta y^+ \leq 1.0$ .

Looking closely at figure 3.2, a small peak can be discerned before the main peak. As the shock becomes stronger, this first peak grows to the same height as the second peak. The dual peak can be explained by the sketch in figure 3.4. When the boundary layer approaches the shock, it separates and a small, thin but stable separation bubble forms. Behind the bubble, a second, much larger, separation bubble is formed. There is a shear layer between the two bubbles where fluid is exchanged between them. The second separation bubble is unstable however and now and again detaches. When it does, the flow behind the first bubble temporarily reattaches, creating the dip in the probability of backflow. The reattached flow meets backwards flowing fluid that fills in for the detached bubble from behind. The flow detaches and a new large separation bubble forms behind the first stable one. The frequency of the separation of the rear bubble is in the order of 2 kHz and is hence not directly coupled to the movement of the innermost part of the shock.

Mean Mach number contours for cases 1–4 are shown in figure 3.5.

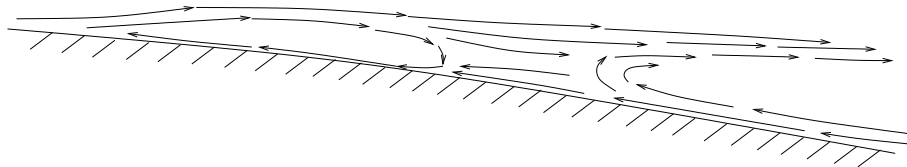
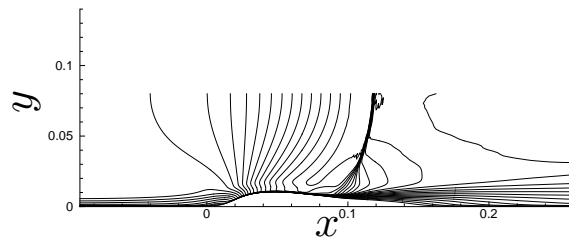
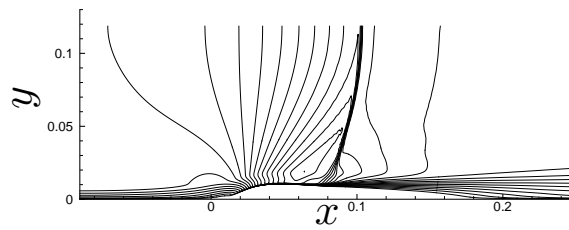


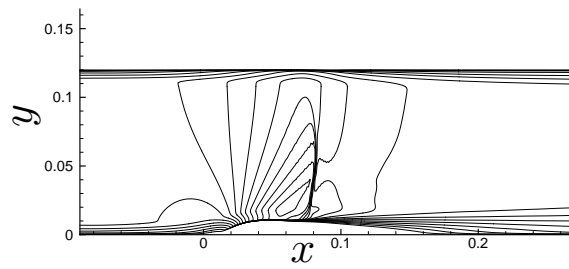
Figure 3.4: Sketch of streamlines at the wall beneath the shock. The height of the first separation bubble is approximately one millimeter.



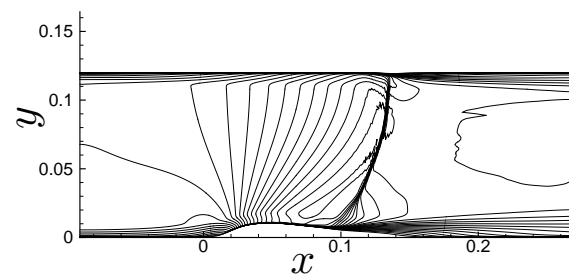
(a) Case 1



(b) Case 2



(c) Case 3



(d) Case 4

Figure 3.5: Mach number contour plots. The inlet free stream Mach number is 0.7 and, the contour level difference is 0.05. The maximum Mach number before the shock is (a) 1.4, (b) 1.3, (c) 1.28, (d) 1.38.

None of the cases features large scale shock movement of the whole shock. The innermost part of the shocks in cases 1, 2 and 4 are however unstable. The standard deviations of the positions of the innermost part of the shocks are between 2 mm and 3.3 mm. The frequencies of the movements are between 350 Hz and 1 kHz. It can be seen by looking at the frequency content of the time correlation between the separation and the shock movement, that the separation triggers the shock movement. By considering that the Strouhal number of the dominating frequency of a phenomenon should be within the range 0.1–0.3 [56, 57, 58, 59], it is argued that the information is carried upstream by elliptic leakage through the boundary layer. The fact that time-space correlations beneath the shock show that frequencies of the separated flow structures are carried upstream strengthen this argument.

The characteristics of the movement of the innermost part of the shocks of case 1 and 2 turned out to be very similar. Both have 350 Hz and 600 Hz as their dominating frequencies, the standard deviations of the shock positions were comparable and the distributions of the shock positions were both bimodal, i. e. the shocks have two preferred positions. Hence, the degree of mass displacement does not seem to have any strong influence on the shock movement in this case.

By considering animations of  $d\bar{p}/dt$  it is concluded that there are no pressure waves that can transport information within the domains considered here which could possibly move the whole shock. Rather, the results of these simulations support the hypothesis of Bogar et al. [60], who presented measurements of transonic SWTBLI. Their wind tunnel was not closed but the air was ejected a distance downstream of the sonic throat. When they altered the length of the test section, Bogar et al. concluded that if the test section was long enough for the upper and lower boundary layers to merge, the frequency of the shock movement scaled with the distance from the shock to the merging point. Otherwise, the frequency of the shock movement scaled with the distance from the shock to the outlet. Biswas [61] used the same domain to make 3D RANS calculations and came to the same conclusion. He added the observation that suction slots in the walls could play the same role as the exit or the merging point of the boundary layers. This theory cannot be confirmed by LES since the computational domain would be much larger than can be handled, at least in the near future.

# Chapter 4

## A new subgrid model

Section 1.5 explained why it is necessary to explore new computational methods. As mentioned there, the focus here will be on developing a new zonal method. In order not to complicate things too much, this development will be presented for incompressible fluids.

### 4.1 Reconstruction of turbulent channel flow

A summary is given here of paper IV included in this thesis. The first step is to develop a method that can reproduce the results of a DNS of turbulent channel flow at Reynolds number 500 based on the channel half height. DNS data  $u, v, w$  and  $p$  are given on a Cartesian grid. A box filter of streamwise and spanwise size  $\Delta x^+ = 196$  and  $\Delta z^+ = 49$  is used to obtain filtered data  $\bar{u}_i$  and  $\bar{p}$  and subgrid stresses  $\tau_{ij}^{tot} = \overline{u_i u_j} - \bar{u}_i \bar{u}_j$ . No filtering is done in the wall normal direction.

In incompressible flow, the spherical part of subgrid stress tensor  $1/3\tau_{kk}^{tot}\delta_{ij}$  is often included in the pressure. The current method is fully capable of modeling the total subgrid stress tensor but, to avoid problems at the matching plane, only the deviatoric part of the subgrid stress tensor,  $\tau_{ij} = \tau_{ij}^{tot} - 1/3\tau_{kk}^{tot}\delta_{ij}$ , will be modeled.

The matching plane is arbitrarily placed at  $y^+ = 62$ . Proper orthogonal decomposition (POD) is used to give the exact representation

$$\tau_{ij}(x, y, z, t) = \sum_{n=1}^{\infty} a^n(x, z, t)\phi_{ij}^n(y) \quad (4.1)$$

of  $\tau_{ij}$  for all cells closer to a wall than 62 viscous units. The orthonormal basis functions,  $\phi_i^n$ , are often referred to as POD modes and  $a^n$  as POD coefficients. More on POD can be found in [62] and [63]. The series is found to be truncatable at mode number 30 with only very small losses of accuracy.

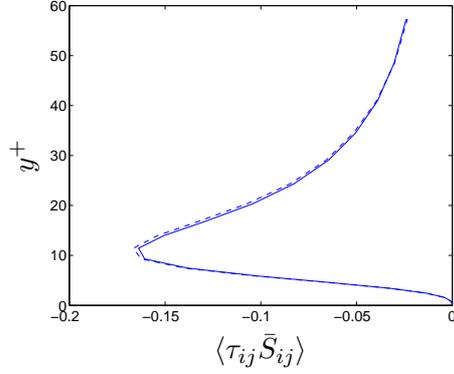


Figure 4.1: Transfer of turbulent kinetic energy to subgrid scales calculated using real stresses (—) and modelled stresses (---).

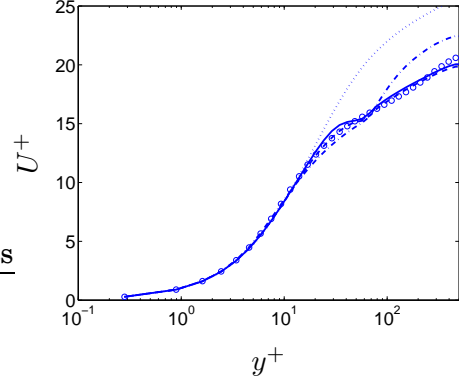


Figure 4.2: Velocity profiles for DNS ( $\circ \circ \circ$ ), pure LES ( $\cdot \cdot \cdot$ ), hybrid LES-RANS ( $-\cdot-$ ) and POD-NN ( $—$ ) and ( $---$ ).

To turn the (truncated) POD representation into a subgrid model, we ask “what values do the POD coefficients assume for a given set of events  $[h^1, \dots, h^M]$ ”. The events are such that they can be calculated from filtered data, for example resolved velocity gradients. Two methods for calculating the most probable values of  $a^n$  given  $[h^1, \dots, h^M]$  are investigated, linear stochastic estimation (LSE) and neural networks (NN). A feed forward NN with two hidden layers is found to be superior to LSE for any given set of events.

*A priori* tests where the events are calculated from filtered DNS data show that the POD-NN system reproduces the correct dynamics of the subgrid stresses. For example, the transfer of turbulent kinetic energy from resolved scales to subgrid scales is shown in figure 4.1.

The POD-NN is implemented in a numerical code and the subgrid stresses below the matching plane are calculated by

$$\hat{\tau}_{ij} = c_b \hat{\tau}_{ij}^{NN} + (1 - c_b) \tau_{ij}^{Smag} \quad (4.2)$$

Mixing is needed to obtain a stable numerical scheme. Outside the matching plane,  $\hat{\tau}_{ij}$  is given by an ordinary Smagorinsky model. van Driest Damping is applied to the Smagorinsky model on both sides of the matching plane. The blending coefficient,  $c_b$ , is set to 0.9 in the greater part of the region except close to the matching plane, where it is damped. Figure 4.2 compares the velocity profiles obtained for two different distributions of  $c_b$  with velocity profiles obtained by pure LES and by an ordinary RANS-LES hybrid scheme. The improvement is remarkable.

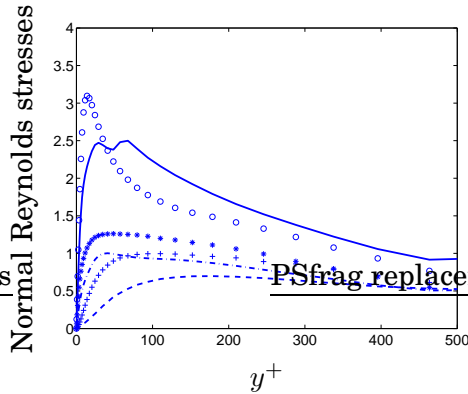


Figure 4.3:  $\circ \circ \circ$ ,  $* * *$  and  $+ + +$  are  $\langle uu \rangle$ ,  $\langle ww \rangle$  and  $\langle vv \rangle$  Reynolds stresses from DNS and  $\text{—}$ ,  $-\cdot-$  and  $- - -$  are resolved  $\langle uu \rangle$ ,  $\langle ww \rangle$  and  $\langle vv \rangle$  Reynolds stresses from a POD-NN calculation.

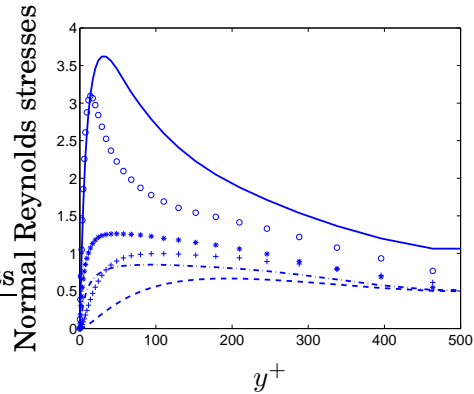


Figure 4.4:  $\circ \circ \circ$ ,  $* * *$  and  $+ + +$  are  $\langle uu \rangle$ ,  $\langle ww \rangle$  and  $\langle vv \rangle$  Reynolds stresses from DNS and  $\text{—}$ ,  $-\cdot-$  and  $- - -$  are resolved  $\langle uu \rangle$ ,  $\langle ww \rangle$  and  $\langle vv \rangle$  Reynolds stresses from the pure LES solution.

The results are not perfect however. This can be seen by looking at the resolved normal Reynolds stresses shown in figure 4.3. For comparison, normal Reynolds stresses obtained from pure LES are shown in figure 4.4, which clearly shows that the pure LES solution has far too high fluctuations in the streamwise direction and very little fluctuation in the other directions. The POD-NN on the other hand has much more realistic levels of resolved streamwise fluctuations, but the  $\langle uu \rangle$  Reynolds stresses show a kink at the matching plane. This kink can also be found in the velocities in figure 4.2. The possible reason is that, despite the damping of the blending coefficient  $c_b$ , there will be a huge jump in modeled shear stresses at the matching plane. The POD-NN system below the matching plane will give stresses at a level consistent with the filter width while the Smagorinsky model outside the matching plane will give far too weak shear stresses. This suggests that the matching plane should be placed further from the wall.

Another possible explanation is that the NN needs some regularization. The network is not trained to handle flow produced by a Smagorinsky model and hence not fitted to deal with the high resolved Reynolds stresses there.

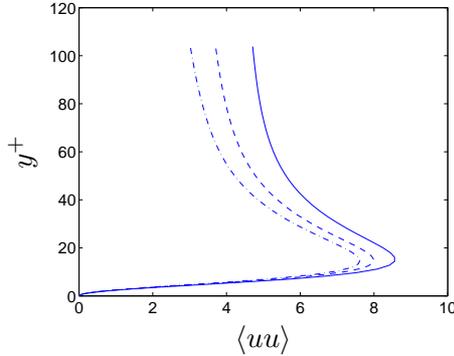


Figure 4.5: Inner scaled  $\langle uu \rangle$  Reynolds stresses from DNS for  $Re = 550$  (---),  $Re = 950$  (-.-) and  $Re = 2000$  (—).

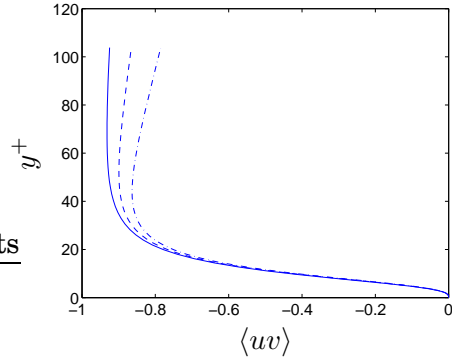


Figure 4.6: Inner scaled  $\langle uv \rangle$  Reynolds stresses from DNS for  $Re = 550$  (---),  $Re = 950$  (-.-) and  $Re = 2000$  (—).

## 4.2 Towards higher Reynolds number

### 4.2.1 Matching plane location

Another POD-NN system was created from DNS of fully developed channel flow of Reynolds number 1000. The DNS at Reynolds number 1000 had the same spanwise resolution as that at Reynolds number 500, but twice the resolution in the streamwise direction and only 10 % stretching in the wall normal direction with  $\min(\Delta y^+) = 0.3$ . The matching plane was placed at a distance of 106 viscous units from the wall.

At the time of the printing of this thesis, this new POD-NN system still contained some errors and therefore, no results are presented. Two trends are however distinguishable. Firstly, it is harder to converge the training of the network. An analysis leading to fewer but statistically more significant events is desirable. Many of the connections in neural networks are usually not needed and some can even be hampering for the performance of the network. This is specially true for large networks and the ones used here are probably no exceptions. There are several methods to identify and remove the unnecessary and/or hampering connections [64] and besides having a stabilizing effect, it can also speed up the network considerably. Secondly, the numerical stability seems to be enhanced compared to having the matching plane at  $y^+ = 60$  and the kink in the velocity profile seems to disappear almost completely. Hopfully more results will be presented in the future.

### 4.2.2 Scaling issues

All variables in this chapter have so far been expressed in viscous units. One advantage is of course that the innermost 10% of the velocity profile is virtually independent of the Reynolds number [26]. The same is not true for the Reynolds stresses, however, as can be seen in figures 4.5 and 4.6. These data are taken from the work of Jimenez et al. [65]. To make the POD-NN system a more general subgrid model, a scaling must be found that makes the Reynolds stresses in the region of interest independent of the Reynolds number. Furthermore, the inner scaling is based on the velocity gradient at the wall and hence is not defined at stagnation points. It would be advantageous to find a scaling that is defined for all type of wall-bounded flows, not only attached boundary layers.



## Chapter 5

# Conclusions and recommendations for future work

This work spans over a fairly wide range of issues in fluid dynamics. There are lessons to be learned in each issue treated here and a great many possibilities for future investigations.

The development of the semi-implicit preconditioning scheme in paper I shows that much of computational resources can be saved by simply using efficient and intelligently chosen numerical methods. The semi-implicit preconditioning scheme was developed to be as accurate as possible but, as discussed in paper I, there are several ways in which it can be made more efficient. The implementation of the scheme also requires some hands on work to ensure that the assumptions of the method are fulfilled. Such checks could be built in into the scheme, and this would enable a variable time step length that would make the scheme both more efficient and accurate.

The numerical investigations of the SWTBLI in papers *II* and *III* show that large scale shock movement in transonic flows is unlikely to be a local phenomenon. The investigations are believed to be very accurate and the results trustworthy, but a few more things can be done to give the simulations even higher credibility.

Firstly, a buffer zone should be added to the outlet. However unlikely it is that the reflected sound waves from the static pressure boundary condition hinder large scale shock movement, their influence cannot be excluded completely until they are removed from the simulations. Secondly, the numerical scheme should be altered. There are more sophisticated shock capturing schemes, and the schemes used for space discretization could be of higher order and/or complemented to include the Leonard stresses. The latter have been shown by Andersson using

the same code to have an influence on the high frequency content of radiated sound [53]. Thirdly, a study should be conducted to determine the role of the Reynolds number. Other studies have shown that, for fixed inlet boundary conditions, there are some effects of the Reynolds number not only on the separation characteristics [66] but also on the angle of attack for which the buffeting phenomenon occurs on transonic wings [67], even though the latter effect is very weak. A study of the influence of Reynolds number would of course require immense computational resources and is probably not possible in the nearest future.

As described in section 2.2.4, the WALE model was modified to make it suitable for compressible flows. However, the values of the constants used are only derived from the Smagorinsky model which, in this work, is of minor importance since the computations were shown to be insensitive to the choice of subgrid model. For future use of the model it would be relevant to make a full investigation of the constants as well as the accuracy of the model.

It would certainly be beneficial to have quantitative, and not only qualitative, experimental data to which to make comparisons. The series of experiments conducted at KTH showed great promise. The work of Olivier Bron [8] ensured repeatability and accuracy of the flow conditions and gave a fairly complete qualitative picture of the flow for different boundary conditions. It is regrettable that this work was not followed up by accurate PIV measurements as was first intended, since the experimental data available are of little use for assessing on the quality of the computations.

The POD-NN subgrid model seems to be able to incorporate much more physics than any other currently available model. The resolved Reynolds stresses are much more consistent with the filter used to derive the equations than in most other models. It is not likely that the model will ever be used in its current form and there is obviously much work to be done on scaling of the components of the model and regularization of the neural network. If these problems can be solved there remains more work to make the model suitable to a wider range of flows. A DNS simulation is necessary for each type of wall-bounded flow that the model is supposed to handle, and the neural network must be trained in some way to distinguish between the flow types. Still, the model shows how elements from different areas of science, in this case POD and neural networks, can be combined to obtain new tools for computations of turbulent flows and that the future of turbulence modeling must perhaps be sought in other fields of mathematics than the prevailing transport equations.

# Appendix A

## Space discretization

This appendix describes in detail how the fluxes are discretized in the G3D code. The description will assume that the grid is Cartesian. If it is not, it can be transformed into a Cartesian one (see for example [52]). All formulations will then apply to the transformed equations instead. This transformation is actually done in the code but will not be described here.

### A.1 Convective fluxes

A purely inviscid flow is governed by Euler's equations, that, if the flow is smooth, can be written in the form

$$\frac{\partial Q}{\partial t} + \frac{\partial F_i}{\partial Q} \frac{\partial Q}{\partial x_i} = 0 \quad (\text{A.1})$$

If only a small area is considered, the flux Jacobian matrices,  $(\partial F_i)/(\partial Q)$ , can be regarded as constants and the linear relation

$$\frac{\partial Q}{\partial t} + \left( \frac{\partial F_i}{\partial Q} \right)_0 \frac{\partial Q}{\partial x_i} = 0 \quad (\text{A.2})$$

is obtained where the subscript 0 denotes evaluation at a reference state. Now assume that this reference state is perturbed with planar waves. These waves are in a plane that has a normal vector  $[\alpha_1, \alpha_2, \alpha_3]$  with  $\alpha_i \alpha_i = 1$ . Aligning the coordinate system with this vector will transform equation (A.2) into

$$\frac{\partial Q}{\partial t} + \hat{A}_0 \frac{\partial Q}{\partial \xi} = 0 \quad (\text{A.3})$$

where

$$\hat{A}_0 = \alpha_i \left( \frac{\partial F_i}{\partial Q} \right)_0$$

and  $\xi$  is the coordinate in the direction of  $\vec{\alpha}$  given by

$$\xi = \alpha_i x_i$$

Equation (A.3) is a system of one dimensional linear equations describing the propagation of waves along the  $\xi$ -axis. The matrix  $\hat{A}_0$  may be diagonalized by its eigenspace vector,  $T$ , using some standard eigendecomposition procedure. This will give

$$T \hat{A}_0 T^{-1} = \Lambda = \text{eigendecomposition}(\lambda_1, \lambda_2, \lambda_3, \lambda_4, \lambda_5) \quad (\text{A.4})$$

The eigenvalues  $\lambda_1, \lambda_2, \lambda_3, \lambda_4, \lambda_5$  are given exactly by

$$\begin{aligned} \lambda_1 &= \alpha_i u_i \\ \lambda_2 &= \lambda_1 \\ \lambda_3 &= \lambda_1 \\ \lambda_4 &= \lambda_1 + a\sqrt{\alpha_i \alpha_i} \\ \lambda_5 &= \lambda_1 - a\sqrt{\alpha_i \alpha_i} \end{aligned} \quad (\text{A.5})$$

where  $a$  is the speed of sound. Using the characteristic variables defined by  $W = T^{-1}Q$ , equation (A.3) can be written as the uncoupled system

$$\frac{\partial W}{\partial t} + \Lambda \frac{\partial W}{\partial \xi} = 0 \quad (\text{A.6})$$

which describes the transport of the characteristic variables  $w_i$  in the  $\xi$ -direction. Each  $w_i$  can be interpreted as a wave carrying some kind of information.  $w_1$  is an entropy wave,  $w_2$  and  $w_3$  are vorticity waves and  $w_4$  and  $w_5$  can be interpreted as sound waves. Each wave transports its information with a characteristic speed described by the corresponding eigenvalue  $\lambda_i$ .

When calculating the fluxes, the code uses the flow variables in primitive form

$$\vec{q} = \begin{bmatrix} \bar{\rho} \\ \tilde{u}_1 \\ \tilde{u}_2 \\ \tilde{u}_3 \\ \bar{p} \end{bmatrix} \quad (\text{A.7})$$

which are obtained from the conservative variables with second order accuracy.  $\bar{p}$  is an approximation calculated by  $\bar{p} = (\gamma - 1)(\bar{p}e_0 + \bar{\rho}(\tilde{u}^2 + \tilde{v}^2 + \tilde{w}^2))$ .

To calculate the inviscid flux over a cell face A, data from four cells are needed. The arrangement is shown in figure A.1. The cell face A is described by the normal vector,  $S_i$ . The outline is to use this  $S_i$  as  $\xi$  in

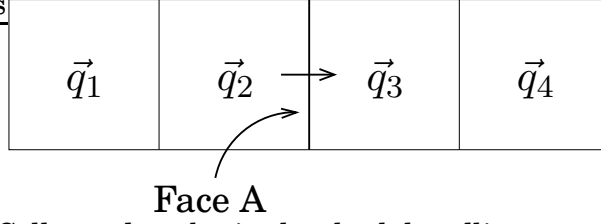


Figure A.1: Cells used to obtain the shock handling term and the inviscid fluxes across the cell face A.

equation (A.3) to obtain the characteristic speeds

$$\begin{aligned}
 \lambda_1 &= \tilde{u}_i^A \mathcal{S}_i \\
 \lambda_2 &= \lambda_1 \\
 \lambda_3 &= \lambda_1 \\
 \lambda_4 &= \lambda_1 + a^A \sqrt{\mathcal{S}_i \mathcal{S}_i} \\
 \lambda_5 &= \lambda_1 - a^A \sqrt{\mathcal{S}_i \mathcal{S}_i}
 \end{aligned} \tag{A.8}$$

where superscript  $A$  denotes that the variable is obtained from  $\vec{q}^A = 0.5(\vec{q}_2 + \vec{q}_3)$ . The sign of each of the eigenvalues determines whether the information is traveling from left to right or from right to left.  $\lambda_i > 0$  indicates the former while  $\lambda_i < 0$  indicates the latter. A left and a right upwinding flux for the cell face A are computed from

$$\begin{aligned}
 \vec{q}^L &= C_1 \vec{q}_1 + C_2 \vec{q}_2 + C_3 \vec{q}_3 + C_4 \vec{q}_4 \\
 \vec{q}^R &= C_4 \vec{q}_1 + C_3 \vec{q}_2 + C_2 \vec{q}_3 + C_1 \vec{q}_4
 \end{aligned} \tag{A.9}$$

The coefficients  $C_1$ ,  $C_2$ ,  $C_3$  and  $C_4$  are derived using a third order polynomial  $\vec{q}(x)$  to represent the variation of the flow state in the normal direction

$$\vec{q}(x) = \vec{A} + \vec{B}x + \vec{C}x^2 + \vec{D}x^3 \tag{A.10}$$

where  $x$  is equal to zero at face A. The face state,  $\vec{q}^L(x=0)$ , is evaluated using the interpolated value,  $\vec{q}(0)$ , modified to include upwinding by adding the third derivative of  $\vec{q}(x)$  according to

$$\begin{aligned}
 \vec{q}^L &= \vec{q}(0) + \delta \frac{\partial^3 \vec{q}}{\partial x^3}(0) = \vec{A} + 6\delta \vec{D} \\
 &= C_1 \vec{q}_1 + C_2 \vec{q}_2 + C_3 \vec{q}_3 + C_4 \vec{q}_4
 \end{aligned} \tag{A.11}$$

where coefficient  $\delta$  in front of the upwind term has been chosen by numerical experiments [68] to be 1/96 to introduce only a small amount of upwinding. This gives

$$(C_1, C_2, C_3, C_4) = \left( -\frac{1}{12} - \delta, \frac{7}{12} + 3\delta, \frac{7}{12} - 3\delta, -\frac{1}{12} + \delta \right) \tag{A.12}$$

which is a scheme that is third order accurate in terms of dissipation but still fourth order in terms of dispersion. By determination of the sign of the corresponding eigenvalue, the characteristic variables are obtained using data from either left or right upwinding, i.e. if  $\lambda_i > 0$ ,  $\vec{q}^L$  is used and if  $\lambda_i \leq 0$ ,  $\vec{q}^R$  is used. The characteristic variables are given by

$$\begin{aligned}
w_1 &= \bar{\rho}^{L/R} - \frac{\bar{p}^{L/R}}{(a^A)^2} \\
w_2 &= \frac{\mathcal{S}_1 \tilde{u}_2^{L/R} - \mathcal{S}_2 \tilde{u}_1^{L/R}}{\sqrt{\mathcal{S}_1 \mathcal{S}_1 + \mathcal{S}_2 \mathcal{S}_2}} \\
w_3 &= \frac{1}{\sqrt{\mathcal{S}_i \mathcal{S}_i}} \left( (\sqrt{\mathcal{S}_1 \mathcal{S}_1 + \mathcal{S}_2 \mathcal{S}_2}) \tilde{u}_3^{L/R} - \mathcal{S}_3 \left( \frac{\mathcal{S}_1 \tilde{u}_1^{L/R} + \mathcal{S}_2 \tilde{u}_2^{L/R}}{\sqrt{\mathcal{S}_1 \mathcal{S}_1 + \mathcal{S}_2 \mathcal{S}_2}} \right) \right) \\
w_4 &= \frac{1}{2} \left( \frac{\bar{\rho}^A \mathcal{S}_i \tilde{u}_i^{L/R}}{a^A \sqrt{\mathcal{S}_i \mathcal{S}_i}} + \frac{\bar{p}^{L/R}}{(a^A)^2} \right) \\
w_5 &= \frac{1}{2} \left( -\frac{\bar{\rho}^A \mathcal{S}_i \tilde{u}_i^{L/R}}{a^A \sqrt{\mathcal{S}_i \mathcal{S}_i}} + \frac{\bar{p}^{L/R}}{(a^A)^2} \right)
\end{aligned} \tag{A.13}$$

The characteristic variables are transformed back to face approximations (denoted  $\hat{\cdot}$ ) of the solution variables in primitive form using

$$\begin{aligned}
\hat{\rho} &= w_1 + w_4 + w_5 \\
\hat{u}_1 &= -\frac{\mathcal{S}_2 w_2}{\sqrt{\mathcal{S}_1 \mathcal{S}_1 + \mathcal{S}_2 \mathcal{S}_2}} - \frac{\mathcal{S}_1}{\sqrt{\mathcal{S}_i \mathcal{S}_i}} \left( \frac{\mathcal{S}_3 w_3}{\sqrt{\mathcal{S}_1 \mathcal{S}_1 + \mathcal{S}_2 \mathcal{S}_2}} - \frac{a^A}{\bar{\rho}^A} (w_4 + w_5) \right) \\
\hat{u}_2 &= \frac{\mathcal{S}_2 w_2}{\sqrt{\mathcal{S}_1 \mathcal{S}_1 + \mathcal{S}_2 \mathcal{S}_2}} - \frac{\mathcal{S}_1}{\sqrt{\mathcal{S}_i \mathcal{S}_i}} \left( \frac{\mathcal{S}_3 w_3}{\sqrt{\mathcal{S}_1 \mathcal{S}_1 + \mathcal{S}_2 \mathcal{S}_2}} - \frac{a^A}{\bar{\rho}^A} (w_4 + w_5) \right) \\
\hat{u}_3 &= \frac{1}{\sqrt{\mathcal{S}_i \mathcal{S}_i}} \left( \frac{w_3}{\sqrt{\mathcal{S}_1 \mathcal{S}_1 + \mathcal{S}_2 \mathcal{S}_2}} + \frac{\mathcal{S}_3 a^A}{\bar{\rho}^A} (w_4 + w_5) \right) \\
\hat{p} &= (a^A)^2 (w_4 + w_5)
\end{aligned} \tag{A.14}$$

These cell face values are then used in the evaluation of  $\mathcal{F}_i^k$  in equation (2.30).

## A.2 Diffusive fluxes

The diffusive fluxes are treated for each cell face with a second order central scheme with no upwinding. That is, if treating the cell face between cell  $i, j, k$  and cell  $i + 1, j, k$ , assuming a Cartesian net, the deriva-

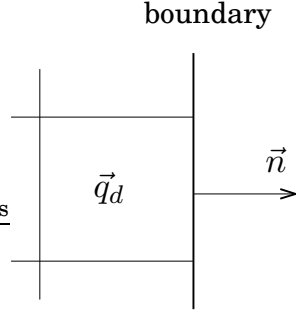


Figure A.2: Treatment of boundary cell using a non-reflective boundary condition.

tives are calculated by

$$\begin{aligned}
 \frac{\partial \vec{q}}{\partial x} &= \frac{\vec{q}_{i+1,j,k} - \vec{q}_{i,j,k}}{x_{i+1,j,k} - x_{i,j,k}} \\
 \frac{\partial \vec{q}}{\partial y} &= \frac{1}{4} \left( \frac{\vec{q}_{i,j+1,k} - \vec{q}_{i,j-1,k}}{y_{i,j+1,k} - y_{i,j-1,k}} \right) + \frac{1}{4} \left( \frac{\vec{q}_{i+1,j+1,k} - \vec{q}_{i+1,j-1,k}}{y_{i+1,j+1,k} - y_{i+1,j-1,k}} \right) \quad (\text{A.15}) \\
 \frac{\partial \vec{q}}{\partial z} &= \frac{1}{4} \left( \frac{\vec{q}_{i,j,k+1} - \vec{q}_{i,j,k-1}}{z_{i,j,k+1} - z_{i,j,k-1}} \right) + \frac{1}{4} \left( \frac{\vec{q}_{i+1,j,k+1} - \vec{q}_{i+1,j,k-1}}{z_{i+1,j,k+1} - z_{i+1,j,k-1}} \right)
 \end{aligned}$$

where  $i, j$  and  $k$  denote the cell indexes in the  $x, y$  and  $z$  directions respectively. These results are then also used in equation (2.30).

### A.3 Extra diffusion for strong shocks

In the case of strong shocks, the scheme previously described cannot handle the discontinuity. Instead, instabilities can cause the calculations to diverge. To prevent this, extra shock handling diffusion is added. The method is developed from the ideas of Jameson et al. [48]. As the fluxes are calculated an extra term with the form

$$C_{PD} \max \left[ \frac{|\bar{p}_1 - 2\bar{p}_2 + \bar{p}_3|}{\bar{p}_1 + 2\bar{p}_2 + \bar{p}_3}, \frac{|\bar{p}_2 - 2\bar{p}_3 + \bar{p}_4|}{\bar{p}_2 + 2\bar{p}_3 + \bar{p}_4} \right] \max[\lambda_i] (\bar{Q}_3 - \bar{Q}_2) \quad (\text{A.16})$$

is added to the right hand side of equation (2.30). In equation (A.16) the indexes of  $\bar{p}$  and  $\bar{Q}$  refer to figure A.1 and index  $i$  on  $\lambda$  refers to equation (A.8). The spectral radius,  $\max[\lambda_i]$ , accounts for aspects of the flow other than the pressure.  $C_{PD}$  is a user defined constant which, if shocks are expected, is normally set to 0.4. In this case, however,  $C_{PD}$  can be set to 0.1 or less.

## A.4 Non-reflective boundary conditions

The plane wave analysis described in A.1 can also be used on a boundary with the normal pointing out of the domain. Since there are no cells outside the domain, some values  $\vec{q}_b$  are prescribed to the boundary. Denoting the values in the cell adjacent to the boundary,  $\vec{q}_d$ , the cell face values are calculated by  $\vec{q}^A = 0.5(\vec{q}_b + \vec{q}_d)$ . The situation is depicted in figure A.2. Then, depending on the sign of the characteristic speeds, components from  $\vec{q}^L = \vec{q}_d$  and/or  $\vec{q}^R = \vec{q}_b$  are used to calculate the characteristic variables.

# Bibliography

- [1] Dolling, D. S., “Fifty Years of Shock-Wave/Boundary-Layer Interaction Research: What Next?” *AIAA Journal*, Vol. 39, No. 8, 2001, pp. 1517 – 1531.
- [2] “Shock-Wave Boundary Layer Interactions,” AGARDograph No.280, 1986.
- [3] Beresh, S. J., Clemens, N. T., and Dolling, D. S., “Relationship Between Upstream Turbulent Boundary-Layer Velocity Fluctuations and Separation Shock Unsteadiness,” *AIAA Journal*, Vol. 40, No. 12, 2002, pp. 2412 – 2422.
- [4] Bur, R., Benay, R., Corbel, B., and Détery, J., “Physical Study of Shock-wave / Boundary-layer interaction control in transonic flow,” AIAA conference, 2000, paper number 2000-0933.
- [5] Sandham, N. D., Yao, Y. F., and Lawal, A. A., “Large-eddy simulation of transonic turbulent flow over a bump,” *International Journal of Heat and Fluid Flow*, Vol. 24, No. 4, 2003, pp. 584 – 595.
- [6] Garnier, E., Sagaut, P., and Deville, M., “Large Eddy Simulation of Shock/Boundary-Layer Interaction,” *AIAA Journal*, Vol. 40, No. 10, 2002, pp. 1935 – 1944.
- [7] Knight, D., Yan, H., Panaras, A. G., and Zheltovodov, A., “Advances in CFD prediction of shock wave turbulent boundary layer interactions,” *Progress in Aerospace Science*, Vol. 39, No. 4, 2003, pp. 121 – 184.
- [8] Bron, O., *Numerical and experimental study of the Shock-Boundary Layer Interaction in Transonic Unsteady Flow*, Ph.D. thesis, Royal Institute of Technology, Sweden, 2003.
- [9] Sigfrids, T., “Hot wire and PIV studies of transonic turbulent wall-bounded flows,” Thesis for licentiate of engineering, Department of Mechanics, Royal Institute of Technology, Sweden, 2003.

- [10] Ichimiya, M., Nakamura, I., and Yamashita, S., "Properties of a re-laminarizing turbulent boundary layer under a favorable pressure gradient," *Experimental Thermal and Fluid Science*, Vol. 17, No. 1–2, 1998, pp. 37 – 48.
- [11] Jones, W. P. and Launder, B. E., "The Prediction of Laminarization with a Two-equation Model of Turbulence," *International Journal of Heat and Mass Transfer*, Vol. 15, No. 2, 1971, pp. 301 – 314.
- [12] Bachalo, W. D. and Johnson, D. A., "Transonic, Turbulent Boundary-Layer Separation Generated on an Axisymmetric Flow Model," *AIAA Journal*, Vol. 24, No. 3, 1986, pp. 437 – 443.
- [13] Moroianu, D., *Numerical Simulations of Turbulent Flows at Widely Different Mach Numbers*, Ph.D. thesis, Lund University, 2003.
- [14] Handa, T. and Masuda, M., "Mechanism of Shock Wave Oscillation in Transonic Diffusers," *AIAA Journal*, Vol. 41, 2003, pp. 64 – 70.
- [15] Thomas, F. O., Putnam, C. M., and Chu, H. C., "On the mechanism of unsteady shock oscillation in shock wave/turbulent boundary layer interactions," *Experiments in Fluids*, Vol. 18, No. 1–2, 1994, pp. 69 – 81.
- [16] Wu, M. and Martin, M. P., "Direct Numerical Simulation of Shock-wave/Turbulent Boundary Layer Interaction," AIAA conference, 2004, paper number 2004-2145.
- [17] Andreopoulos, J. and Muck, K. C., "Some new aspects of the shock-wave/boundary-layer interaction in compression-ramp flows," *AIAA Journal*, Vol. 180, 1987, pp. 405 – 428.
- [18] Deck, S., "Numerical Simulation of Transonic Buffet over a Supercritical Airfoil," *AIAA Journal*, Vol. 43, 2005, pp. 1556 – 1566.
- [19] Xiao, Q. and Tsai, H. M., "Numerical Study of Transonic Buffet on a Supercritical Airfoil," *AIAA Journal*, Vol. 44, 2006, pp. 620 – 628.
- [20] Lee, B. H. K., "Oscillation Shock Motion Caused by Transonic Shock Boundary-Layer Interaction," *AIAA Journal*, Vol. 28, 1990, pp. 942 – 944.
- [21] Robinson, D. F., Harris, J. E., and Hassan, H. A., "Unified Turbulence Closure Model for Axisymmetric and Planar Free Shear Flows," *AIAA Journal*, Vol. 33, 1995, pp. 2325 – 2331.
- [22] Menter, F. R., "Two-Equation Eddy-Viscosity Turbulence Models for Engineering Applications," *AIAA Journal*, Vol. 32, 1994, pp. 1598 – 1605.

- [23] Menter, F. R., Egorov, Y., and Rusch, D., “Steady and Unsteady Flow Modelling Using the  $k-\sqrt{k}L$  Model,” *Turbulence, Heat and Mass Transfer 5*, edited by K. Hanjalić, Y. Nagano, and S. Jakirlić, Dubrovnic, Croatia, 2006, pp. 403 – 406.
- [24] Sinha, K., Mahesh, K., and Candler, G. V., “Modeling the Effect of Shock Unsteadiness in Shock/Turbulent Boundary-Layer Interactions,” *AIAA Journal*, Vol. 43, 2005, pp. 586 – 594.
- [25] Thivet, F., Knight, D., Zheltovodov, A., and Maksimov, A., “Insights in Turbulence Modeling for Crossing-Shock-Wave/Boundary-Layer Interactions,” *AIAA Journal*, Vol. 39, 2001, pp. 985 – 994.
- [26] Pope, S. B., *Turbulent flows*, Cambridge university press, Cambridge, United Kingdom, 2000.
- [27] “Introduction to the modelling of Turbulence,” von Karman Institute for Fluid Dynamics Lecture Series 2000-04, 2000.
- [28] Kravchenko, A. G. and Moin, P., “On the Effect of Numerical Errors in Large Eddy Simulations of Turbulent Flows,” *Journal of Computational Physics*, Vol. 131, 1997, pp. 310 – 322.
- [29] Urbin, G. and Knight, D., “Large-Eddy Simulation of Supersonic Boundary Layer Using an Unstructured Grid,” *AIAA Journal*, Vol. 39, 2001, pp. 1288 – 1295.
- [30] von Kaenel, R., Kleiser, L., Adams, N. A., and Vos, J. B., “Large-Eddy Simulation of Shock-Turbulence Interaction,” *AIAA Journal*, Vol. 42, 2004, pp. 2516 – 2528.
- [31] “Workshop on Refined Turbulence Modeling,” 11th ERCOF-TAC/IAHR Workshop, 2005.
- [32] Davidson, L. and Peng, S.-H., “Hybrid LES-RANS: a one-equation SGS model combined with a  $k - \omega$  model for predicting recirculating flows,” *International Journal of Numerical Methods in Fluids*, Vol. 43, 2003, pp. 1003–1018.
- [33] Hamba, F., “A Hybrid RANS/LES Simulation of Turbulent Channel Flow,” *Theoretical and Computational Fluid Dynamics*, Vol. 16, 2003, pp. 387 – 403.
- [34] Tucker, P. G. and Davidson, L., “Zonal  $k - l$  based large eddy simulations,” *Computers & Fluids*, Vol. 33, 2004, pp. 267 – 287.

- [35] Larsson, J., Lien, F. S., and Yee, E., “Large Eddy Simulation of High Reynolds Number Channel Flow on Coarse Grids,” *13th Annual Conference of the Computational Fluid Dynamics Society of Canada*, St. Johns, Newfoundland, Canada, 2005, pp. 61–68.
- [36] Davidson, L. and Dahlström, S., “Hybrid LES-RANS: An approach to make LES applicable at high Reynolds number,” *International Journal of Computational Fluid Dynamics*, Vol. 19, 2005, pp. 415–427.
- [37] Davidson, L. and Billson, M., “Hybrid LES-RANS using synthesized turbulent fluctuations for forcing in the interface region,” *International Journal of Heat and Fluid Flow*, Vol. in print, 2006.
- [38] Piomelli, U., Balaras, E., Pasinato, H., Squires, K. D., and Spalart, P. R., “The inner-outer layer interface in large-eddy simulations with wall-layer models,” *International Journal of Heat and Fluid Flow*, Vol. 24, 2003, pp. 538 – 550.
- [39] Temmerman, L., Leschziner, M. H. M. A., and Hanjalić, K., “A hybrid two-layer URANS-LES approach for large eddy simulation at high Reynolds number,” *International Journal of Heat and Fluid Flow*, Vol. 26, 2005, pp. 173 – 190.
- [40] Ghosal, S., “Mathematical and Physical Constraints on Large-Eddy Simulation of Turbulence,” *AIAA Journal*, Vol. 37, 1999, pp. 425 – 433.
- [41] Eriksson, L.-E., “Development and validation of highly modular flow solver versions in g2dflow and g3dflow series for compressible viscous reacting flow,” Internal report 9970–1162, Volvo Aero Corporation, Sweden, 1995.
- [42] Erlebacher, G., Hussaini, M. Y., Speziale, C. G., and Zang, T. A., “Toward the large-eddy simulation of compressible turbulent flows,” *Journal of Fluid Mechanics*, Vol. 238, 1992, pp. 155 – 185.
- [43] Larsson, J., “Numerical Simulation of Turbulent flows for Turbine Blade Heat Transfer Applications,” Thesis for the degree of doctor of philosophy, Department of Thermo and Fluid Dynamics, Chalmers University of Technology, Sweden, 1998.
- [44] Speziale, C. G., Erlebacher, G., Zang, T. A., and Hussaini, M. Y., “The subgrid-scale modeling of compressible turbulence,” *AIAA Journal*, Vol. 31, 1988, pp. 940 – 942.
- [45] Schlichting, H. and Gersten, K., *Boundary-Layer Theory*, 8th edition, Springer-Verlag, Berlin Heidelberg, 2000.

- [46] Nicoud, F. and Ducros, F., “Subgrid-Scale Stress Modelling Based on the Square of the Velocity Gradient Tensor,” *Flow, Turbulence and Combustion*, Vol. 62, No. 3, 1999, pp. 183 – 200.
- [47] Schlichting, H., *Boundary-Layer Theory, seventh edition*, McGraw-Hill Book Company, New York, USA, 1979.
- [48] Jameson, A., Schmidt, W., and Turkel, E., “Numerical Solutions of the Euler Equations by Finite Volume Methods Using Runge-Kutta Time-Stepping Schemes,” AIAA paper, 1981, paper number 81-1259.
- [49] Eriksson, L.-E., “Transfinite Mesh Generation and Computer-Aided Analysis of Mesh Effects,” Thesis for the degree of doctor of philosophy, Department of Computer Sciences, Uppsala University, Sweden, 1984.
- [50] Ørbekk, E., *Algebraic and elliptic grid generation for CFD applications*, Ph.D. thesis, Universitetet i Trondheim, Norges tekniske høgskola, 1994.
- [51] Laney, C. B., *Computational Gasdynamics*, Cambridge University Press, New York, USA, 1998.
- [52] Hoffmann, K. A. and Chiang, S. T., *Computational fluid dynamics for engineers volume II*, Engineering Education System, Wichita, Kansas, USA, 1993.
- [53] Andersson, N., *A Study of Subsonic Turbulent Jets and Their Radiated Sound Using Large-Eddy Simulation*, Ph.D. thesis, Chalmers University of Technology, 2005.
- [54] Bogey, C. and Bailly, C., “Three-dimensional non-reflective boundary conditions for acoustic simulations: far field formulation and validation test case,” *Acta Acustica united with Acustica*, Vol. 88, 2002, pp. 463 – 471.
- [55] Johansson, G. and Castillo, L., “LDA measurements in turbulent boundary layers with zero pressure gradient,” *Proc. Turbulence and Shear Flow Phenomena, 2<sup>nd</sup> International Symposium*, edited by E. Lindborg, A. Johansson, J. Eaton, J. Humphrey, N. Kasagi, M. Leschziner, and M. Sommerfeld, Stockholm, Sweden, 2001, pp. 15 – 20.
- [56] White, F. M., *Viscous Fluid Flow*, McGraw-Hill, 2006.
- [57] Krajnović, S. and Davidson, L., “Numerical Study of the Flow Around a Bus-Shaped Body,” *Journal of Fluids Engineering*, Vol. 125, 2003, pp. 500 – 509.

- [58] Krajnović, S. and Davidson, L., “Flow Around a Simplified Car Part 1: Large Eddy Simulation,” *Journal of Fluids Engineering*, Vol. 127, 2005, pp. 907 – 918.
- [59] Billson, M., *Computational Techniques for Turbulence Generated Noise*, Ph.D. thesis, Chalmers University of Technology, 2004.
- [60] Bogar, T. J., Sajben, M., and Kroutil, J. C., “Characteristic Frequencies of Transonic Diffuser Flow Oscillations,” *AIAA Journal*, Vol. 9, 1983, pp. 1232 – 1240.
- [61] Biswas, D., “Unsteady 3-D Navier-Stokes Simulations of Characteristic Frequency and Length Scales in Transonic Diffuser,” AIAA conference, 2004, paper number 2004-2715.
- [62] Holmes, P., Lumley, J. L., and Berkooz, G., *Turbulence, Coherent Structures, Dynamical Systems and Symmetry*, Cambridge Monographs on Mechanics, 1996.
- [63] George, W. K., “Some thoughts on similarity, the POD, and finite boundaries,” *Trends in Mathematics*, edited by A. Gyr and A. Tsinobler, 1998, pp. 117 – 128.
- [64] Haykin, S., *Neural Networks*, Prentice Hall International, Inc., international ed., 1999.
- [65] “<http://torroja.dmt.upm.es/ftp/channels/>,” DNS turbulent channel data, 2006.
- [66] Laurent, J., “Interaction onde de choc/chouche limite à grand nombre de Reynolds. Measure sur la paroi plane.” PV-25, ONERA, France, 1977.
- [67] Bartels, R. E., “Flow and Turbulence Modeling and Computation of Shock Buffet Onset for Conventional and Supercritical Airfoils,” TP-1998-206908, NASA, Langley Reserch Center, Hampton, Virginia, 1998.
- [68] Mårtensson, H., Eriksson, L.-E., and Albråten, P., “Numerical Simulations of Unsteady Wakeflow,” Conf. Proc. 10th ISABE meeting, 2001.

# Paper I



## Paper II



## Paper III



## Paper IV